SCATTERING OF LINEAR AND WEAKLY NONLINEAR WAVES: PSEUDOSPECTRAL APPROACHES

by

YONGZE CHEN and PHILIP L.-F. LIU

CENTER FOR APPLIED COASTAL RESEARCH

Department of Civil Engineering
University of Delaware
Newark, Delaware 19716

Scattering of linear and weakly nonlinear waves: Pseudospectral approaches

Yongze Chen and Philip L.-F. Liu

School of Civil and Environmental Engineering

Cornell University, Ithaca, NY 14853

Abstract

Wave propagation models for linear and weakly nonlinear waves are developed based on mild-slope equations. The pseudospectral Fourier approach is used to reduce mild-slope equations to a set of ordinary differential equations in terms of the modified potential, $\phi\sqrt{CC_g}$, at the collocation points in the on-offshore direction. The wave field is then decoupled into a series of angular modes including all the forward and backward propagation modes. Both forward and backward wave fields are taken into account in the case of linear waves. For weakly nonlinear waves only the forward scattering is considered. Linear and nonlinear small-angle parabolic models are also developed for comparison. The effects of energy dissipation, which are nonlinear, are directly included in the formulation. Numerical results are presented for wave refraction over an equilibrium beach profile and wave focusing over submerged shoals: an elliptic shoal on a sloping beach and a circular shoal on a flat bottom. The importance of the backward scattering is illustrated by the latter example.

1 Introduction

In recent years parabolic approximations have been employed to develop efficient and practical models for computing propagation of water waves over a varying topography. Liu (1990) gave a detailed account of the development and the capability of various parabolic approximation models. The early versions of parabolic approximation models require that waves propagate nearly along a predetermined direction. In other words, these models can only provide accurate solutions in the forward propagation wave field within a relatively narrow range of angular spectrum; this is called small-angle approximation. Efforts have been made by several researchers to relax this limitation with various degrees of success. Most recently, Dalrymple & Kirby (1988) and Dalrymple et al. (1989) developed a wave propagation model valid for a large angle of incidence. In their models the wave field is decomposed into an angular spectrum via a Fourier transformation in the alongshore direction. Ignoring the backward scattering field, Dalrymple and his associates retained

1

all the angular modes in the forward propagation wave field independent of the angle of incidence.
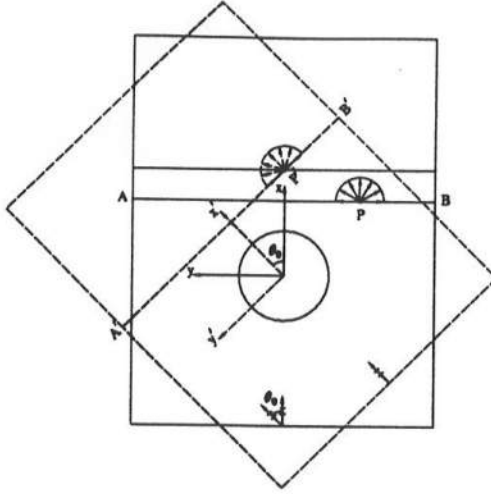

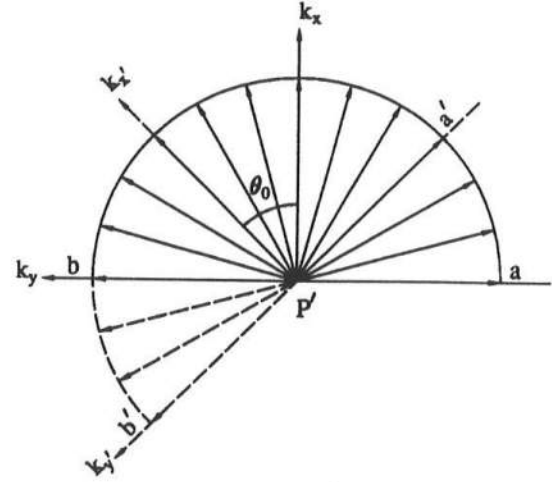Fig. 1a Sketch of the axisymmetry of the wave field behind a submerged circular shoal.

Fig. 1b Forward propagation modes at a point P' with respect to different coordinate systems.

For many refraction-diffraction problems, the existing wide-angle parabolic models, without including the backward propagation wave field, do not necessarily give accurate solutions. For instance, consider the scattering of a small amplitude wave train by a submerged circular shoal. As shown in Figure 1a, the x-axis coincides with the on-offshore direction. Independent of the angle of incidence, the existing wide-angle models calculate the forward propagation angular modes with propagation directions covering the range from $-90°$ to $90°$, e.g. wave field at a point P shown in Figure 1a. If the height of the submerged shoal is not very large in comparison with the depth, the reflection is indeed weak and can be neglected. The existing wide-angle models provide accurate solutions for the normal incidence ($\theta_0 = 0$). On the other hand, for an oblique incidence, the direction of wave propagation coincides with $x'-$axis and the wave field at point P' is exactly the same as that at point P due to the axisymmetry of the circular shoal (i.e. line $A'B'$ corresponds to line AB in Figure 1a). Hence, the wave field at point P' should be expressed as the linear combination of forward propagation modes with respect to coordinate system (x', y'),

whose propagation directions span from a' to b' in Figure 1b. However, the existing wide-angle parabolic models express the wave field at point P' in terms of forward propagation modes with respect to the coordinate system (x, y), whose propagation directions span from a to b as shown in Figure 1b. Therefore, the accuracy of the existing wide-angle parabolic models depends on the significance of angular modes ranging from b to b', which in turn depends on the variation of the topography in y-direction. If the contribution from these modes is not small, the existing wide-angle parabolic models can not give accurate results, even if the reflection is negligible. Furthermore, because the angular span from b to b' is directly proportional to the angle of incidence, less accurate results are expected from the existing wide-angle parabolic models for the cases with larger angle of incidence. In summary, for a large angle of incidence, a portion of the forward propagation wave field in terms of the coordinate system (x', y') is actually in the backward propagation field in terms of the coordinate system (x, y), which is adopted in numerical computations. Hence, the existing wide-angle models, which ignore the backward propagation wave field, can not simulate this situation accurately. One possible remedy is to rotate the coordinates such that the direction of incident wave propagation always coincide with the x-axis (a similar idea has been suggested by Dodd (1989) who treated the reflected wave as a part of the forward propagation wave field). However, for a general problem with a complex topography one does not necessarily know how to choose the x-direction. A more formal way to deal with this problem is to include the backward propagation wave field in the model. In so doing, the weakly reflection is also included in the computation.

Based on the small-angle approximation, Liu & Tsay (1983) developed an iterative numerical model which included the backward propagation wave field. McMaken (1986) pointed out that Liu & Tsay's approach can not be extended to the wide-angle approximation, i.e. the iterative scheme diverges if higher order derivative terms are included in the parabolic approximation. Therefore, a new approach is needed to model the forward and backward wave fields without the constraint of the small-angle approximation.

Because the Fourier transformation was used in Dalrymple's and his associate's models,

only linear problems can be solved directly. Although the nonlinearity of Stokes waves was incorporated in their computations by using an empirical nonlinear dispersion relationship, their approach cannot be extended to include other types of nonlinearity in governing equations. Using a method of multiple scales and Stokes expansions for the velocity potential and free-surface displacement, Suh et al. (1990) developed an angular spectrum model for the propagation of Stokes waves over a mildly-varying topography. This model includes nonlinearity in a more rigorous fashion, but it still can not incorporate nonlinear terms due to energy dissipation.

In this paper we would like to accomplish two objectives. First, we shall present a mathematical model to calculate both forward and backward propagation wave fields for linear waves. The angular spectrum scheme is used. Therefore, the model is valid for all angles of incidence. Secondly, we shall consider some nonlinearities in the model. The nonlinearity may be contributed from the finite amplitude effects of Stokes waves or from energy dissipation, such as bottom friction and wave breaking. Because these nonlinear terms are derived either analytically or empirically for the forward propagation modes, the nonlinear model ignores the backward scattering wave field.

In the following sections we begin with the introduction of a nonlinear mild-slope equation. We then apply the pseudospectral Fourier method by representing the wave field in terms of trigonometric polynomials in the alongshore (y-) direction. (A similar pseudospectral method has been used by Panchang & Kopriva (1989) who employed the Chebyshev collocation pseudospectral method in both horizontal directions to solve the Euler's equations.) The mild-slope equation is converted into a set of coupled nonlinear ordinary differential equations for the modified potential at the collocation points. Because the coupling matrix is real and symmetric, the wave field can be decoupled into a series of angular modes including all the forward and backward propagation components. For linear waves both forward and backward scattering wave fields are solved by constructing a Bremmer series. Only the forward scattering is considered for weakly nonlinear waves (the corresponding model is called wide-angle parabolic model). This is primarily because of our

4

ignorance in splitting the nonlinearity between the forward and the backward propagation wave fields. For comparison, small-angle models are also derived for both linear and nonlinear waves.

Several numerical examples are presented to demonstrate the validity of both small-angle and wide-angle parabolic models and the importance of the backward scattering field. In the first example, the wave refraction over an equilibrium beach profile (parallel depth contours) is examined. It is shown that the wide-angle parabolic model produces the same results as those of ray theory for all angles of incidence up to $90°$. The small-angle model can be employed only when the angle of incidence is less than $30°$. The nonlinear effects due to breaking and bottom friction are also examined. In the second and the third examples, wave focusing over a submerged shoal is investigated. For the case of an elliptical shoal, the comparison between numerical results and experimental data (Berkhoff, Booij & Radder 1982) shows that nonlinearity is important in the focal region and the small-angle model produces excellent numerical results for this particular experimental set-up. To examine the importance of the backward scattering field and the range of validity of the nonlinear wide-angle parabolic model, the wave focusing behind a circular shoal resting on a flat bottom is studied. Because of the axisymmetry of the circular shoal, the wave pattern behind the shoal should be independent of the angle of incidence. For linear waves, if backward scattering is ignored, the wave pattern for a large angle of incidence ($\theta_0 = 60°$ in the numerical example) shows significant difference from that for the normal incidence. However, if both forward and backward scattering are taken into account, the numerical results show that the wave pattern indeed is independent of the angle of incidence. For nonlinear waves, only forward scattering is considered and the nonlinear wide-angle parabolic model can produces satisfying results for angles of incidence up to $60°$.

2 Linear and nonlinear mild-slope equations

The propagation of small amplitude water waves over a slowly varying topography can be described by the following linear mild-slope equation (Berkhoff 1972, Smith & Sprinks 1975)

$$\nabla \cdot (CC_g \nabla \phi) + k^2 CC_g \phi = 0 \qquad (2.1)$$

where $\phi(x, y)$ is the velocity potential on the mean free surface ($z = 0$), $k(x, y)$ is the wave number, $C = \omega/k$ and $C_g = d\omega/dk$ are the phase and group velocities respectively, ω is the wave angular frequency, which is related to the wave number $k(x, y)$ and the water depth $h(x, y)$ by the dispersion relation

$$\omega^2 = gk \tanh kh \qquad (2.2)$$

where g is the gravitational acceleration.

The corresponding non-linear mild-slope equation has not been formally derived. However, if the direction of wave propagation can be predetermined (e.g. forward propagation only), the mild-slope equation with a weak nonlinearity caused by the finite amplitude can be written approximately as (Liu 1990):

$$\nabla \cdot (CC_g \nabla \phi) + k^2 CC_g \phi - \mathcal{K} \left(\frac{\omega}{g}\right)^2 |\phi|^2 \phi = 0 \qquad (2.3)$$

in which

$$\mathcal{K} = \frac{k^4 C^2}{8\sinh^4 kh}(8 + \cosh 4kh - 2\tanh^2 kh) \qquad (2.4)$$

We reiterate here that the cubic nonlinear term was derived based on the assumption that the dominant wave propagation direction coincides with x-axis. Therefore, the application of the mild-slope equation in the nonlinear form should be restricted to the forward propagation wave field.

The effects of energy dissipation have also been included in the mild-slope equation by many researchers (Booij 1981, Dingemans 1983, 1985, Liu 1986, Liu & Tsay 1985,

Dalrymple et al. 1984). Denoting W as the rate of energy dissipation per unit wave energy, we introduce the dissipative term into the mild-slope equation

$$\nabla \cdot (CC_g \nabla \phi) + k^2 CC_g \phi + i\omega W \phi - \mathcal{K} \left(\frac{\omega}{g}\right)^2 |\phi|^2 \phi = 0 \qquad (2.5)$$

where $i = \sqrt{-1}$. The dissipation function W is usually defined empirically according to different dissipative processes, and is a function of wave amplitude, i.e. $W = W(x, y; \phi)$. This adds another nonlinear term to the mild-slope equation. Once again, the empirical forms for the dissipation function W are largely developed for forward progressive waves. The nonlinear mild-slope equation, (2.5), should be used for the forward propagation modes.

Introducing the transformation

$$\xi = \phi \sqrt{CC_g} \qquad (2.6)$$

into linear and nonlinear mild-slope equation (2.1) and (2.5), we obtain

$$\nabla^2 \xi + k_c^2 \xi + G(x, y; \xi)\xi = 0 \qquad (2.7)$$

where

$$k_c^2 = k^2 - \frac{\nabla^2 \sqrt{CC_g}}{\sqrt{CC_g}} \qquad (2.8)$$

and

$$G(x, y; \xi) = 0 \qquad (2.9)$$

for linear waves, or

$$G(x, y; \xi) = \frac{1}{CC_g} \left[i\omega W(x, y; \xi/\sqrt{CC_g}) - \mathcal{K} \left(\frac{\omega}{g}\right)^2 \frac{|\xi|^2}{CC_g} \right] \qquad (2.10)$$

for nonlinear problems with the explicit expression depending on the specific form used

for the dissipative function W.

3 Pseudospectral Fourier method

In this paper we consider periodic problems in the alongshore (y-) direction with a length L. We map the interval $y \in [0, L]$ into $\bar{y} \in [0, 2\pi]$. The variables in the new domain are indicated by an overbar, i.e.

$$\xi(x, y) = \bar{\xi}(x, \bar{y}), \quad k_c(x, y) = \bar{k}_c(x, \bar{y}), \quad G(x, y; \xi) = \bar{G}(x, \bar{y}; \bar{\xi}) \tag{3.1}$$

The mild-slope equation can be rewritten as (after overbars have been dropped for simplicity)

$$\frac{\partial^2 \xi}{\partial x^2} + \left(\frac{2\pi}{L}\right)^2 \frac{\partial^2 \xi}{\partial y^2} + k_c^2 \xi + G\xi = 0 \tag{3.2}$$

for $y \in [0, 2\pi]$. Because ξ is a periodic function in the y-direction, it can be interpolated by trigonometric polynomial interpolants

$$g_j(y) = \frac{1}{2N} \sin[N(y - y_j)] \cot(\frac{y - y_j}{2}) \qquad (j = 0, 1, \ldots, 2N - 1) \tag{3.3}$$

at the following set of collocation points (Gottlieb et al. 1984)

$$y_j = \frac{\pi j}{N} \qquad (j = 0, 1, \ldots, 2N - 1) \tag{3.4}$$

Thus, ξ has the form

$$\xi(x, y) = \sum_{j=0}^{2N-1} \xi(x, y_j) g_j(y) \tag{3.5}$$

For later use, the m-th order derivative of ξ with respect to y, evaluated at the collocation point $y = y_n$ is given here

$$\left.\frac{\partial^m \xi(x, y)}{\partial y^m}\right|_{y=y_n} = \sum_{j=0}^{2N-1} \xi(x, y_j) \left.\frac{d^m g_j(y)}{dy^m}\right|_{y=y_n} = \sum_{j=0}^{2N-1} [D_m]_{n,j} \psi_j(x) \tag{3.6}$$

where

$$\psi_j(x) = \xi(x, y_j) \tag{3.7}$$

and

$$[D_m]_{n,j} = \frac{d^m g_j(y)}{dy^m}\bigg|_{y=y_n} \tag{3.8}$$

which is a $2N \times 2N$ matrix. Specifically (Gottlieb et al. 1984),

$$[D_1]_{n,j} = \begin{cases} \frac{1}{2}(-1)^{n+j} \cot(\frac{y_n - y_i}{2}), & j \neq n \\ 0, & j = n \end{cases} \tag{3.9}$$

and

$$[D_2]_{n,j} = \begin{cases} \frac{1}{2}(-1)^{n+j+1} \csc^2(\frac{y_n - y_i}{2}), & j \neq n \\ -\frac{2N^2+1}{6}, & j = n \end{cases} \tag{3.10}$$

From (3.9) and (3.10), D_1 is a real anti-symmetric matrix and D_2 is a real symmetric matrix. In general, the m-th order ($m > 2$) spectral differentiation operator can be written as the $m/2$-th power of D_2 if m is even or as the m-th power of D_1 if m is odd.

Substituting (3.5) into (3.2) and evaluating the resulting equation at each collocation point, y_n, we obtain

$$\frac{d^2\psi_n}{dx^2} + \left(\frac{2\pi}{L}\right)^2 \sum_{j=0}^{2N-1} [D_2]_{n,j}\psi_j + k_n^2\psi_n + G_n\psi_n = 0 \quad (n = 0, 1, \ldots, 2N-1) \tag{3.11}$$

where

$$k_n(x) = k_c(x, y_n), \qquad G_n(x, \psi_n) = G(x, y_n; \psi_n) \tag{3.12}$$

It is remarked here that $g_j(y_n) = \delta_{jn}$ has been employed. We have converted the mild-slope equation into a system of coupled nonlinear ordinary differential equations for $\psi_n(x)$. The coupling is provided by the second derivative of the modified potential function with respect to the y-axis (the alongshore direction). Since the coupling matrix D_2 is symmetric, the solution to (3.11) can be expressed as a linear combination of a series of forward and

backward propagating modes. In the following section, for a linear wave system, we take both forward and backward wave propagation into account by constructing the Bremmer series from the resulting Helmholtz-like equations. On the other hand, only the forward propagation shall be considered for weakly nonlinear waves.

4   Fourier decomposition

To decompose the wave field into a series of wave modes which consist of a complete discrete angular spectrum, we rewrite (3.11) in the following form:

$$\frac{d^2\psi_n}{dx^2} + \left(\frac{2\pi}{L}\right)^2 \sum_{j=0}^{2N-1} [D_2]_{n,j}\psi_j + K^2\psi_n - K^2\nu_n^2\psi_n + G_n\psi_n = 0 \qquad (4.1)$$

where

$$\nu_n^2(x) = 1 - k_c^2(x, y_n)/K^2(x), \qquad K^2(x) = \frac{1}{2\pi}\int_0^{2\pi} k_c^2(x,y)dy \qquad (4.2)$$

in which K^2 denotes the averaged value of k_c^2 over the computational domain in the y-direction. This transformation was first used by Dalrymple et al. (1989).

Because D_2 is a real symmetric matrix, there exists an orthogonal matrix Q such that

$$Q^T D_2 Q = I\left\{-\lambda^2\right\} \qquad (4.3)$$

where Q^T is the transpose of Q, I is a $2N \times 2N$ identity matrix and $\{-\lambda^2\}$ is a $2N$ column vector called the spectrum of D_2, whose n-th element, $-\lambda_n^2 (n = 0, 1, \ldots, 2N - 1)$, is the n-th eigenvalue of D_2. The eigenvalues and the corresponding eigenvectors can be given analytically. The spectrum of D_2 can be written as:

$$\left\{-\lambda^2\right\} = \left\{0, -1, -1, \ldots, -(N-1)^2, -(N-1)^2, -N^2\right\}^T \qquad (4.4)$$

Therefore, with the exception of the first and the last eigenvalues, $-\lambda_n^2 = 0$ and $-N^2$,

10

the other eigenvalues of D_2 have double multiplicity. The corresponding $2N$ mutually orthogonal eigenvectors are

$$\vec{V}_n = \{\exp[i(n - N)y_0], \exp[i(n - N)y_1], \ldots, \exp[i(n - N)y_{2N-1}]\}^T \qquad (4.5)$$

with $n = 0, 1, \ldots, 2N - 1$. Hence, the matrix Q in (4.3) can be written explicitly as

$$\sqrt{N}Q = \begin{bmatrix} \frac{1}{\sqrt{2}} & \cos y_0 & \sin y_0 & \cdots & \cos[(N-1)y_0] & \sin[(N-1)y_0] & \frac{1}{\sqrt{2}}\cos N y_0 \\ \frac{1}{\sqrt{2}} & \cos y_1 & \sin y_1 & \cdots & \cos[(N-1)y_1] & \sin[(N-1)y_1] & \frac{1}{\sqrt{2}}\cos N y_1 \\ \vdots & \vdots & \vdots & \vdots & \vdots & \vdots & \vdots \\ \frac{1}{\sqrt{2}} & \cos y_{2N-1} & \sin y_{2N-1} & \cdots & \cos[(N-1)y_{2N-1}] & \sin[(N-1)y_{2N-1}] & \frac{1}{\sqrt{2}}\cos N y_{2N-1} \end{bmatrix}$$

$$(4.6)$$

We introduce the following non-singular transformation

$$\psi_n(x) = \sum_{m=0}^{2N-1} Q_{n,m}\eta_m(x) \qquad (n = 0, 1, \ldots, 2N - 1) \qquad (4.7)$$

Substituting (4.7) into (4.1) and multiplying the resulting equations by Q^T, noting that $Q^T Q = I$, yield

$$\frac{d^2\eta_n}{dx^2} + \left[K^2 - \left(\frac{2\pi}{L}\right)^2 \lambda_n^2\right]\eta_n + \sum_{j=0}^{2N-1} H_{n,j}\eta_j = 0 \qquad (4.8)$$

where

$$H_{n,j} = \sum_{m=0}^{2N-1} Q_{m,n}\left[G_m(x; \sum_{l=0}^{2N-1} Q_{m,l}\eta_l) - K^2\nu_m^2\right]Q_{m,j} \qquad (4.9)$$

We now split the wave field into the forward propagation and the backward propagation fields

$$\eta_n = \eta_n^+ + \eta_n^- \qquad (4.10)$$

11

$$\frac{d\eta_n^+}{dx} = i\sqrt{K^2 - \left(\frac{2\pi}{L}\right)^2 \lambda_n^2} \ \eta_n^+ + P_n(\eta_0^+, \ldots, \eta_{2N-1}^+; \eta_0^-, \ldots, \eta_{2N-1}^-) \qquad (4.11)$$

$$\frac{d\eta_n^-}{dx} = -i\sqrt{K^2 - \left(\frac{2\pi}{L}\right)^2 \lambda_n^2} \ \eta_n^- - P_n(\eta_0^+, \ldots, \eta_{2N-1}^+; \eta_0^-, \ldots, \eta_{2N-1}^-) \qquad (4.12)$$

Substituting (4.10)–(4.12) into (4.8), we obtain

$$P_n = \frac{i}{2\sqrt{K^2 - \left(\frac{2\pi}{L}\right)^2 \lambda_n^2}} \left[i\frac{dK^2}{dx} \frac{\eta_n^+ - \eta_n^-}{2\sqrt{K^2 - \left(\frac{2\pi}{L}\right)^2 \lambda_n^2}} + \sum_{j=0}^{2N-1} H_{n,j}\eta_j \right] \qquad (4.13)$$

Equations (4.11) and (4.12) are coupled first-order nonlinear ordinary differential equations. The coupling between the forward and the backward propagation is represented by P_n.

4.1   Wide-angle parabolic model

Neglecting the backward scattering η_n^- as a first approximation, (4.8) can be simplified as

$$\frac{d\eta_n^+}{dx} = i\sqrt{K^2 - \left(\frac{2\pi}{L}\right)^2 \lambda_n^2} \ \eta_n^+ + \frac{i}{2\sqrt{K^2 - \left(\frac{2\pi}{L}\right)^2 \lambda_n^2}} \left[i\frac{dK^2}{dx} \frac{\eta_n^+}{2\sqrt{K^2 - \left(\frac{2\pi}{L}\right)^2 \lambda_n^2}} \right.$$
$$\left. + \sum_{j=0}^{2N-1} H_{n,j}^+\eta_j^+ \right] \qquad (n = 0, 1, \ldots, 2N-1) \qquad (4.14)$$

where

$$H_{n,j}^+ = \sum_{m=0}^{2N-1} Q_{m,n} \left[G_m(x; \sum_{l=0}^{2N-1} Q_{m,l}\eta_l^+) - K^2\nu_m^2 \right] Q_{m,j} \qquad (4.15)$$

Note that for each forward propagating mode η_n^+ the direction of wave propagation can be expressed as

12

$$\theta_n = \tan^{-1}\left[\frac{\left(\frac{2\pi}{L}\right)\lambda_n}{\sqrt{K^2 - \left(\frac{2\pi}{L}\right)^2\lambda_n^2}}\right] \qquad (n = 0, 1, \ldots, 2N-1) \qquad (4.16)$$

The corresponding forward propagating wave field at each collocation point ψ_n includes contributions from $2N$ modes whose angles sweep from $-90°$ to $90°$ (see (4.7)). Therefore, (4.14) with (4.7) is called "wide-angle" parabolic model. We remark that the derivation of the wide-angle model is independent of the angle of incidence. In the appendix we show that if the angle of incidence coincides with one of θ_n in (4.16) the linear wide-angle model gives the same result as the ray theory does.

On the right-hand side of (4.14), the first term represents either a progressive mode or an evanescent mode depending on whether $[K^2 - \left(\frac{2\pi}{L}\right)^2\lambda_n^2]$ is positive or negative. The second term represents the shoaling and refraction effect of each wave mode. The third term denotes the wave diffraction due to uneven topography in the y-direction and nonlinearities due to finite wave amplitude and/or energy dissipation if $G \neq 0$.

4.2   Bremmer series solution to linear wave propagation

As discussed in the introduction section, for a large angle of incidence the backward scattering may become important if the variation of the topograph in y-direction is not small (see (4.9), (4.13) and (4.12)) . In this section we derive Bremmer series solutions to (4.8) to include both the forward and backward wave field.

Let $\eta_{n,0}^{\pm}(x)$ satisfy

$$\eta_{n,0}^- = 0 \qquad (n = 0, 1, \ldots, 2N-1) \qquad (4.17)$$

$$\frac{d\eta_{n,0}^+}{dx} = i\sqrt{K^2 - \left(\frac{2\pi}{L}\right)^2\lambda_n^2}\,\eta_{n,0}^+ + P_n(\eta_{0,0}^+, \ldots, \eta_{2N-1,0}^+; \eta_{0,0}^-, \ldots, \eta_{2N-1,0}^-)$$

$$\eta_{n,0}^+(0) = a_n \qquad (n = 0, 1, \ldots, 2N-1) \qquad (4.18)$$

and $\eta_{n,m}^{\pm}(x)$ $(m \geq 1)$ satisfy

$$\frac{d\eta_{n,m}^-}{dx} = -i\sqrt{K^2 - \left(\frac{2\pi}{L}\right)^2 \lambda_n^2}\, \eta_{n,m}^- - P_n(\eta_{0,m-1}^+, \ldots, \eta_{2N-1,m-1}^+; \eta_{0,m}^-, \ldots, \eta_{2N-1,m}^-)$$

$$\eta_{n,m}^-(b) = 0 \qquad (n = 0, 1, \ldots, 2N-1) \qquad (4.19)$$

$$\frac{d\eta_{n,m}^+}{dx} = i\sqrt{K^2 - \left(\frac{2\pi}{L}\right)^2 \lambda_n^2}\, \eta_{n,m}^+ + P_n(\eta_{0,m}^+, \ldots, \eta_{2N-1,m}^+; \eta_{0,m}^-, \ldots, \eta_{2N-1,m}^-)$$

$$\eta_{n,m}^+(0) = 0 \qquad (n = 0, 1, \ldots, 2N-1) \qquad (4.20)$$

where a_n is the n-th forward propagating mode of the incident wave at $x = 0$ and b is the length of computational domain in the x-direction, then

$$\eta_n^+(x) = \sum_{m=0}^{\infty} \eta_{n,m}^+(x) \qquad (n = 0, 1, \ldots, 2N-1) \qquad (4.21)$$

$$\eta_n^-(x) = \sum_{m=0}^{\infty} \eta_{n,m}^-(x) \qquad (n = 0, 1, \ldots, 2N-1) \qquad (4.22)$$

yield solutions to (4.11) and (4.12), provided that these Neumann series converge absolutely and uniformly. Furthermore, if we define

$$U_{n,2m}(x) = \eta_{n,m}^+(x), \quad U_{n,2m+1} = \eta_{n,m+1}^-(x) \quad (m = 0, 1, \ldots) \qquad (4.23)$$

then

$$\eta_n(x) = \sum_{m=0}^{\infty} U_{n,m}(x) = \eta_n^+(x) + \eta_n^-(x) \qquad (n = 0, 1, \ldots, 2N-1) \qquad (4.24)$$

are the Bremmer series and will, subject to absolute and uniform convergence, give the solution to (4.8). Note that the first term ($m = 0$) in the series (4.24) indeed is the solution to (4.14), which is the parabolic approximation to equation (4.8).

In the study of one-dimensional wave propagation in an inhomogeneous medium, Atkinson (1960) gave the specific necessary and sufficient condition, in terms of the variability of the medium, for the absolute and uniform convergence of the Bremmer series. Loosely

14

speaking, the series will converge if the variations in the medium (equivalently, the variations of wave number) are not too large. In the case when the bathymetry contours are straight lines, parallel to the alongshore direction, without taking any nonlinear effects into account, equation (4.8) is automatically decoupled into $2N$ one-dimensional Helmholtz equations, governing the wave propagation of each mode in the discrete angular spectrum. Therefore, we expect the $2N$ Bremmer series in (4.24) will converge because of the mild-slope assumption.

5   Small-angle parabolic model

For the purpose of comparison, we also derive a small-angle parabolic model and record it here. Assume that the forward and the backward waves propagate primarily in the $\pm x$-direction, respectively. The wave field can be split in the following way:

$$\psi_n = \psi_n^+ + \psi_n^- \tag{5.1}$$

$$\frac{d\psi_n^+}{dx} = ik_n\psi_n^+ + P_n \tag{5.2}$$

$$\frac{d\psi_n^-}{dx} = -ik_n\psi_n^- - P_n \tag{5.3}$$

Substitutions of (5.1),

(5.2) and (5.3) into (3.11) yield

$$P_n = \frac{i}{2k_n}\left[i\frac{dk_n}{dx}(\psi_n^+ - \psi_n^-) + \left(\frac{2\pi}{L}\right)^2 \sum_{j=0}^{2N-1}[D_2]_{n,j}\psi_j + G_n(x;\psi_n)\psi_n\right] \tag{5.4}$$

Ignoring the backward wave ψ_n^-, which usually is small, we have

$$\frac{d\psi_n^+}{dx} = ik_n\psi_n^+ + \frac{i}{2k_n}\left[i\frac{dk_n}{dx}\psi_n^+ + \left(\frac{2\pi}{L}\right)^2 \sum_{j=0}^{2N-1}[D_2]_{n,j}\psi_j^+ + G_n(x;\psi_n^+)\psi_n^+\right]$$

$$(n = 0, 1, \ldots, 2N - 1) \tag{5.5}$$

15

which is a system of first-order ordinary differential equations for the forward wave field. When $G = 0$ (linear theory), (5.5) recovers the parabolic equation for the forward propagation wave field derived by Radder (1979).

We can further factor out the fast variable in ψ_n^+ by introducing

$$\psi_n^+(x) = \Psi_n^+(x) \exp(ik_0^* x) \tag{5.6}$$

into (5.5)

$$\frac{d\Psi_n^+}{dx} = i(k_n - k_0^*)\Psi_n^+ + \frac{i}{2k_n}\left[i\frac{dk_n}{dx}\Psi_n^+ + \left(\frac{2\pi}{L}\right)^2 \sum_{j=0}^{2N-1} [D_2]_{n,j}\Psi_j^+ + G_n\Psi_n^+ \right]$$
$$(n = 0, 1, \ldots, 2N - 1) \tag{5.7}$$

where k_0^* is a constant reference wave number.

6 Energy dissipation

When waves propagate into shallow water, the effects of bottom friction and wave breaking may become significant. To incorporate these energy dissipation effects into the mild-slope equation, analytic expression for W in terms of ϕ must be specified. For different physical processes, different forms of empirical expression of W have been proposed. When energy dissipation is caused by the bottom turbulent boundary layer, the dissipation function W may be expressed as (Liu & Tsay, 1985)

$$W = \frac{16 f_e \omega k^2 C_g |\phi|}{3\pi g(2kh + \sinh 2kh)\sinh kh} \tag{6.1}$$

where f_e is the friction factor, which should be related to wave parameters and bottom conditions. For simplicity, we choose f_e as a constant.

In the case of wave breaking, the wave height decay model developed by Dally et al. (1984) is applied and the dissipation function W can be expressed as (Kirby & Dalrymple

16

$$W = \frac{JC_g}{h}\left[1 - \left(\frac{gh\Gamma}{2\omega|\phi|}\right)^2\right] \qquad (6.2)$$

where J and Γ are empirical constants. Calibrating with laboratory data, Dally et al. recommended that $J = 0.15$ and $\Gamma = 0.4$ should be used. For convenience, the "0.78 criterion" is used to provide prediction of incipient breaking, i.e. waves start breaking when $\frac{H}{h} > 0.78$, where H is the wave height.

7 Numerical examples

To solve the first-order ordinary differential equations (4.14) and (5.7), initial conditions are needed. For a uniform incident wave the free surface displacement ζ is given along $x = 0$, i.e.

$$\zeta = A_0 \exp(ik_0 \sin\theta_0 y) \qquad (7.1)$$

where A_0, k_0 and θ_0 are the incident amplitude, wave number and the angle of incidence along $x = 0$, respectively. For the small-angle model, the free surface displacement of the incident waves is converted into a set of initial conditions as:

$$\Psi_n^+(0) = \psi_n^+(0) = -i\frac{\omega}{g}A_0\sqrt{C_0 C_{g0}}\exp\left\{ik_0 \sin\theta_0 \frac{nL}{2N}\right\} \quad (n = 0, 1, \ldots, 2N-1) \qquad (7.2)$$

where C_0 and C_{g0} are the phase and the group velocity along $x = 0$, respectively. For the wide-angle model, the corresponding initial conditions are

$$\eta_n^+(0) = \sum_{j=0}^{2N-1} Q_{j,n}\psi_j^+(0) \qquad (n = 0, 1, \ldots, 2N-1) \qquad (7.3)$$

where $\psi_j^+(0)$ are the same as (7.2). Note that in (4.18) $a_n = \eta_n^+(0)$. When $\theta_0 \neq 0$, the periodic condition in the y-direction requires

$$L = \frac{2\pi}{k_0 \sin\theta_0}p \qquad (7.4)$$

17

where $p \neq 0$ and is an arbitrary integer.

The fourth-order Runge-Kutta method is employed to solve equations (5.7) and (4.14) and to obtain the Bremmer series solutions ((4.18) to (4.20)). To test the capability of the present models for various physical phenomena such as refraction, diffraction, nonlinearity caused by finite amplitude and energy dissipation and to examine the importance of the backward scattering field for a large angle of incidence, we apply the models to several different cases. These include wave refraction over an equilibrium beach, and wave focusing behind submerged elliptic and circular shoals. Bottom friction and breaking are not considered in the following examples unless specifically indicated otherwise.

7.1 Wave refraction over an equilibrium beach profile

When the bathymetry contours are parallel to the alongshore direction and there is no obstacle inside the domain, the diffraction effect vanishes. Furthermore, if the reflection is ignored, results from the ray theory should be recovered from the mild-slope equation (Berkhoff, 1976). To verify this point with present models, we have chosen an equilibrium beach profile, which represents a typical natural beach profile along the east coast of the U.S. (Dean, 1977). The equilibrium beach profile used in numerical experiments is given as

$$h(x) = 0.15(1000 - x)^{2/3} \qquad (7.5)$$

in which both the on-offshore coordinate x and depth h have a unit in meter. The incident wave period is $T = 8$ second and wave amplitude $A_0 = 1.0m$. The computational domain in the x-direction is $1000(m)$ and in the y-direction $L = \left[\frac{1000 k_0 \sin \theta_0}{2\pi}\right] \times \frac{2\pi}{k_0 \sin \theta_0}$ (m) in which $[f]$ denotes the nearest integer to the real number f inside the bracket, θ_0 is the angle of incidence and k_0 is the incident wave number. When the incident wave is normal incident, $L = 1000(m)$. We have taken $N = 20$, $\Delta x = 10m$ and the reference wave number in (5.7) as k_0. The comparison among results from the wide-angle and the small-angle parabolic models and the ray theory is shown in figure 2. In this figure, the wave amplitude has been normalized by the incident amplitude for different angles of incidence. The numerical

18

results obtained from the wide-angle model show excellent agreement with those from the ray theory for angles of incidence up to 89° (the analytic proof of this agreement is given in the appendix). The small-angle model, on the other hand, can give good approximation only when the angle of incidence is less than 30°. In fact, when water depth varies only in the x-direction, the amplitude given by the linear small-angle model are independent of the angle of incidence. This can be proved from (5.5) and is shown in the following.
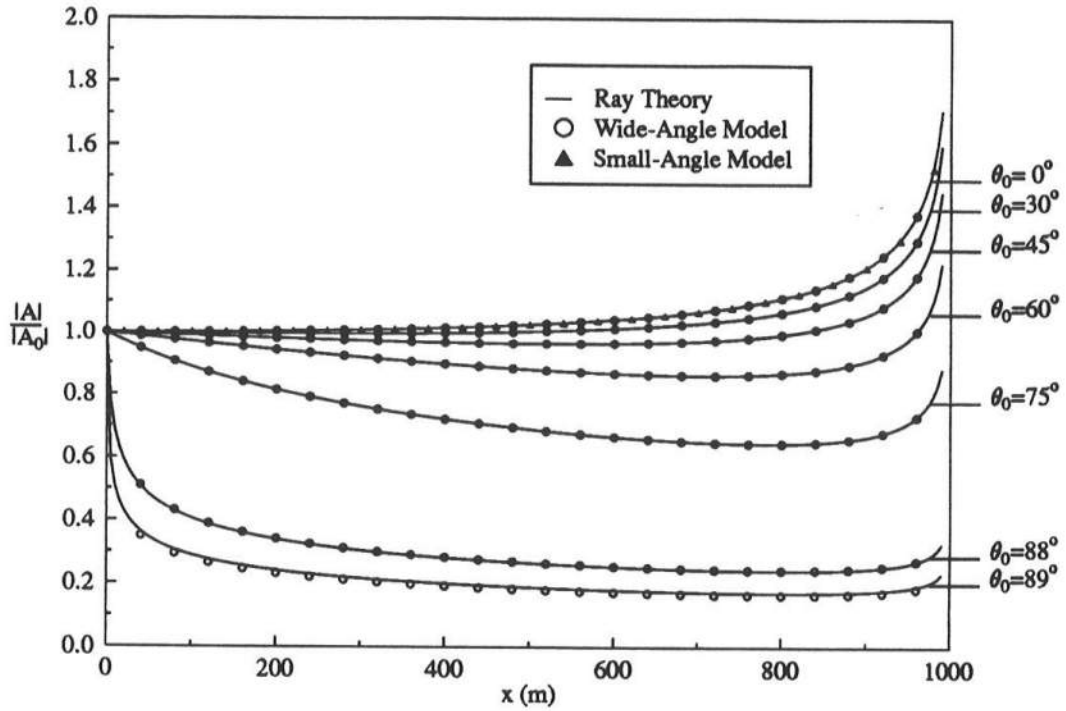
Figure 2: Amplitude variation over an equilibrium beach profile for different angles on incidence.

Because the wave amplitude is uniform in the y-direction in this case, the solution to (5.5) can be written as:

$$\xi(x,y) = A(x)\exp\left[ik_y(x)y\frac{L}{2\pi}\right] = \sum_{n=0}^{2N-1}\psi_n(x)g_n(y) \qquad (7.6)$$

where $k_y(x)$ is a real value. The second derivative of (7.6) with respect to y evaluated at y_n becomes:

$$\left.\frac{\partial^2 \xi(x,y)}{\partial y^2}\right|_{y=y_n} = -\left(k_y \frac{L}{2\pi}\right)^2 A \exp\left[ik_y(x)y\frac{L}{2\pi}\right] = \sum_{j=0}^{2N-1} [D_2]_{n,j}\psi_j(x) \qquad (7.7)$$

We want to show that $|\xi| = |A|$ is independent of the angle of incidence.

Substituting (7.6) and (7.7) into (5.5), and noting that $k_n = k_c$, we obtain

$$\frac{dA}{dx} = i\left[k_c - \frac{nL}{2N}\frac{dk_y}{dx} - \frac{k_y^2}{2k_c}\right]A - \frac{A}{2k_c}\frac{dk_c}{dx} \qquad (7.8)$$

Integrating the above equation yields

$$A(x) = \frac{D}{\sqrt{k_c}}\exp\left[\int_0^x \left(k_c - \frac{nL}{2N}\frac{dk_y}{dx} - \frac{k_y^2}{2k_c}\right)dx\right] \qquad (7.9)$$

where D is a constant. Therefore, the amplitude ratio with respect to the incident amplitude can be written as

$$\frac{|A|}{|A_0|} = \frac{\sqrt{k_{c0}}}{\sqrt{k_c}} \qquad (7.10)$$

which is independent of the angle of incidence, i.e. the angle of incidence has impact on the phase of ξ but not on the amplitude of ξ. Furthermore (7.10) can be shown as a good approximation to the shoaling formula. Using the relationships among $|\zeta|$, $|\phi|$, and $|\xi|$, we have

$$\frac{|\zeta|}{|\zeta_0|} = \frac{|\phi|}{|\phi_0|} = \frac{|\xi/\sqrt{CC_g}|}{|\xi_0/\sqrt{C_0C_{g0}}|} = \frac{|A/\sqrt{CC_g}|}{|A_0/\sqrt{C_0C_{g0}}|} = \frac{\sqrt{k_{c0}C_0C_{g0}}}{\sqrt{k_cCC_g}} \qquad (7.11)$$

The second term on the right-hand side of (2.8) is usually very small. Neglecting it, we have $k_{c0}C_0 = k_cC$ and (7.11) becomes

$$\frac{|\zeta|}{|\zeta_0|} = \frac{\sqrt{C_{g0}}}{\sqrt{C_g}} \qquad (7.12)$$

which is the well-known shoaling formula.

Figure 3 shows numerical results using different friction factors ($f_e = 0.0, 0.02, 0.05$)
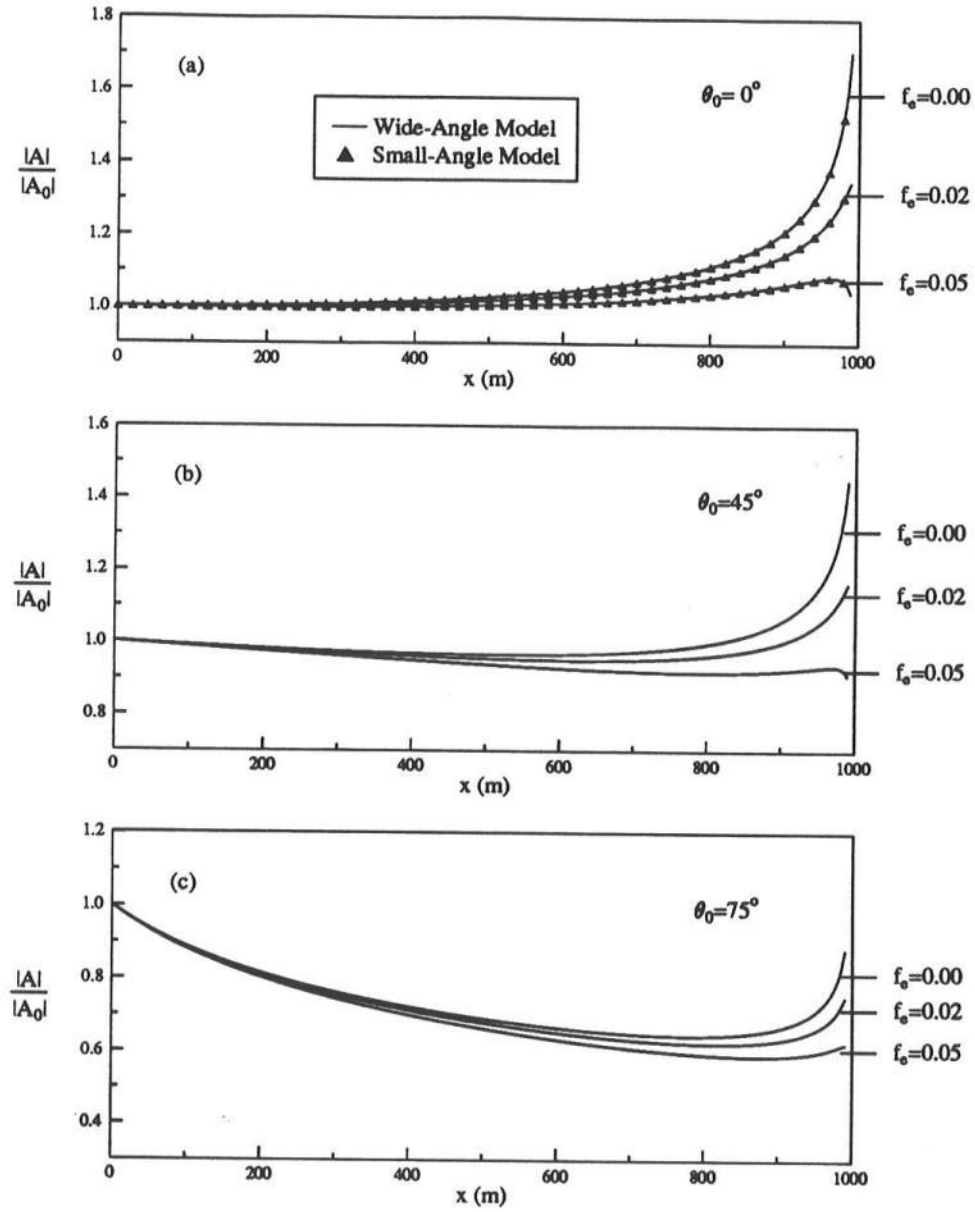
Figure 3: Numerical results of normalized wave amplitude using different friction factors for different angles of incidence.

for different angles of incidence ($\theta_0 = 0°, 45°, 75°$). The bottom friction reduces the wave amplitude significantly in the shallow-water region, especially when f_e is large, and therefore postpones wave breaking. Comparing figure 3a, 3b and 3c, we observe that for the same friction factor, the dissipation function W in (6.1) reduces the wave amplitude more quickly for the wave with a small angle of incidence than the wave with a large angle of incidence. For a normal incident wave, both small-angle and wide-angle models agree very well (figure 3a).

Figure 4 gives the results of breaking wave height variation in the surf zone. The wave is normal incident and the bottom friction is also taken into account ($f_e = 0.02$). The breaking criteria $(\frac{H}{h})_b = 0.78$ is used to locate the position of incipient wave breaking. Equation (6.2) is then employed in the models. This figure shows that after breaking the wave amplitude decreases dramatically.
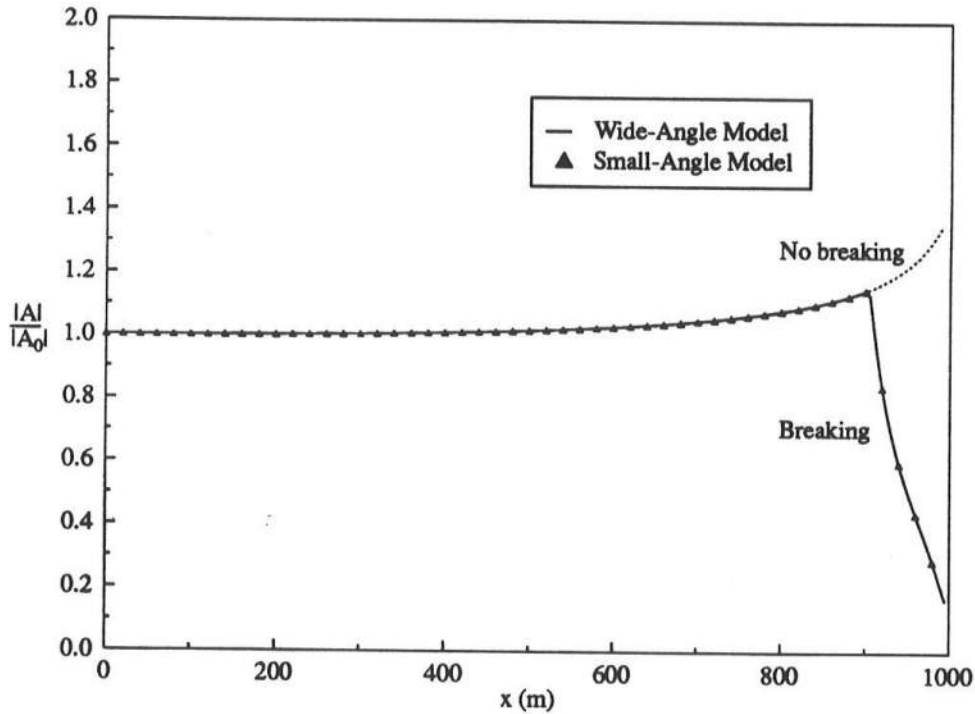
Figure 4: Prediction of breaking wave amplitude in surf zone for a normal incident wave with friction factor $f_e = 0.02$.

22

7.2   Wave focusing behind an elliptic shoal on a sloping beach

To test the present models for an irregular topography, we have used the experiment reported by Berkhoff, Booij & Radder (1982). The experimental bathymetry consists of an elliptic shoal situating on a plane beach with a slope 1:50. The slope rises from a region of constant depth $h = 0.45m$ and the entire slope is rotated clockwise at an angle of $20°$ as shown in figure 5, where the solid lines indicate bottom contours and dashed lines are the transects (labelled from 1 to 8) along which data from the experiment of Berkhoff et al. (1982) are available. To give more detail of the geometry of the shoal, we introduce slope-oriented coordinates (x', y') as shown in figure 5 , which are related to computational coordinates (x, y) by

$$x' = (x - 10.5)\cos 20° - (y - 10.0)\sin 20°$$
$$y' = (x - 10.5)\sin 20° + (y - 10.0)\cos 20°$$

(7.13)
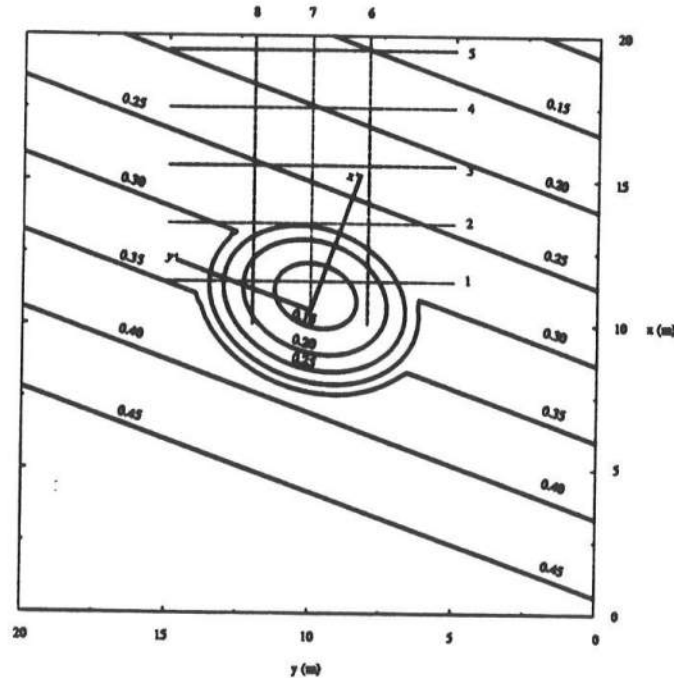
Figure 5: Bathymetry of the computational domain for the experiment by Berkhoff et al. (1982). Dashed lines indicate the transects of wave measurement.

The origin $(x', y') = (0, 0)$ corresponds to the center of the shoal and the boundary of the shoal is given by

$$(x'/3)^2 + (y'/4)^2 = 1 \tag{7.14}$$

Outside the shoal region, the water depth is given by

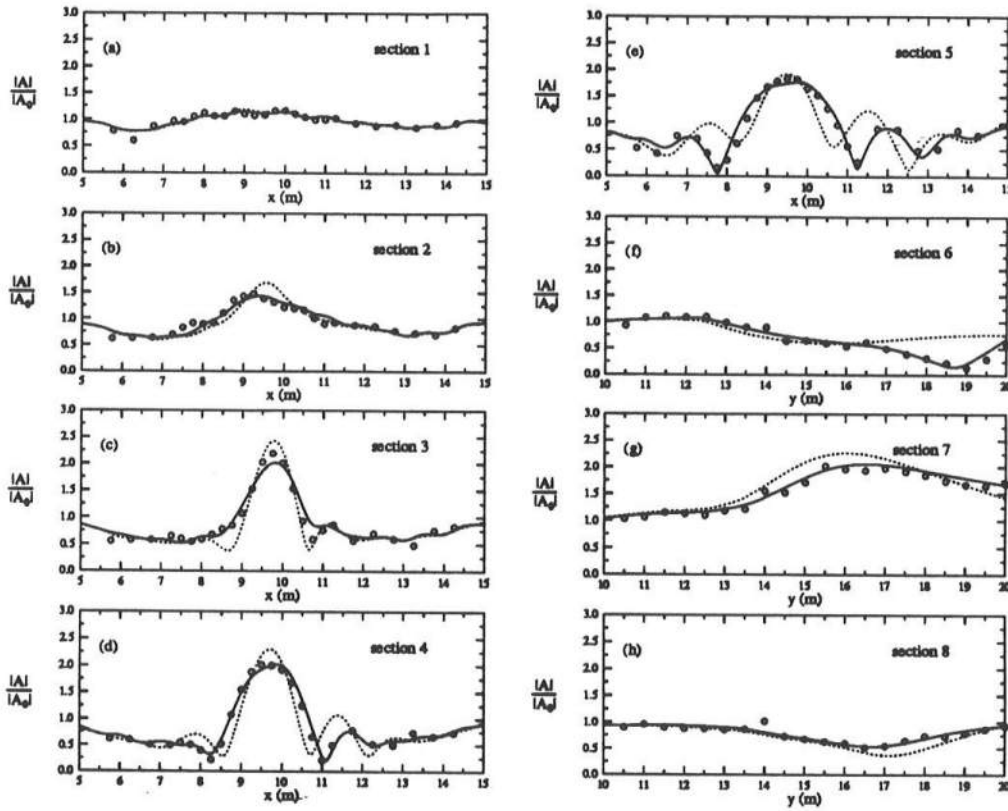$$h = \begin{cases} h_0 = 0.45m, & x' < -5.84m \\ h_0 - 0.02(5.84 + x')m, & x' \geq -5.84m \end{cases} \tag{7.15}$$

Figure 6: Comparison between the small-angle model results with the experimental data by Berkhoff et al. (1982) at section 1–8 (see Fig.5) in terms of normalized wave amplitude: —— nonlinear model; ···· linear model; ○ ○ ○ experimental data.

In the shoal region the depth is modified according to

$$h = h + 0.3 - 0.5\sqrt{1 - (x'/3.75)^2 - (y'/5)^2} \qquad (7.16)$$

resulting in a depth at the center of the shoal of $0.1332m$.

The initial conditions specify normal incident waves with a period $T = 1s$ and an amplitude $A_0 = 0.0232m$. For the small-angle model, we have taken $\Delta x = 0.5m$ and $N = 20$ (i.e. $\Delta y = 0.5m$). Both linear and nonlinear (due to finite amplitude) models are used to calculate the transformation of the incident wave. Comparisons among numerical solutions from these models and the laboratory measurements along the transects 1–8 are shown in figure 6. Again the wave amplitude has been normalized by the incident wave amplitude. In figure 6 numerical results from the nonlinear and linear small-angle model are indicated by solid and dotted lines, respectively, while measured data are indicated by open circles. The nonlinear small-angle model shows excellent agreement with the measured data. The nonlinearity due to finite amplitude clearly plays an important role in wave focusing behind the shoal.

For the wide-angle model, we have taken $\Delta x = 0.5m$ and $N = 15$ (i.e. $\Delta y = 0.67m$). The nonlinear results are shown in figure 7 by the solid lines, while the measured data are indicated by open circles. Very good agreement between numerical results and experimental data is observed.

Following Dalrymple et al. (1989), we present quantitative comparison between experimental data and numerical results using a statistical parameter proposed by Willmott (1981). As a measure of the degree to which a numerical model's predictions are error-free, Willmott introduced a dimensionless quantity, d, as an index of agreement

$$d = 1 - \frac{\sum_{i=1}^{M}(P_i - O_i)^2}{\sum_{i=1}^{M}(|P_i - O_i| + |O_i - \bar{O}|)^2} \qquad (7.17)$$

where $\bar{O}$ is the mean of the observed variates O_i and P_i ($i = 1, \ldots, M$) are the predicted variates. The values for d vary between 0.0 and 1.0, where 1.0 indicates perfect agreement

25

between observations and predictions and 0.0 indicates complete disagreement. The indices
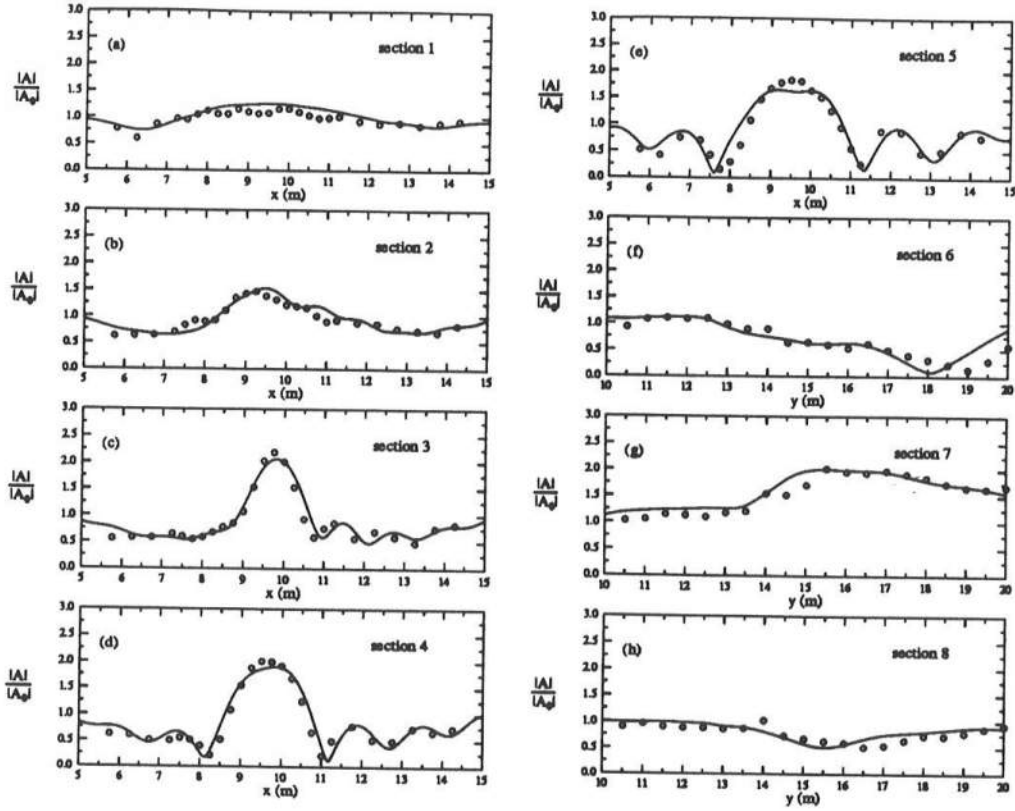

Figure 7: Comparison between the nonlinear wide-angle model results with the experimental data by Berkhoff et al. (1982) in terms of normalized wave amplitude: —— model results; o o o experimental data.

of agreement between numerical results from each nonlinear model and the experimental data along each transect shown in figures 6 and 7 as well as for total measurement points are given in table 1. Numerical results from the Dalrymple et al.'s (1989) wide-angle model and from the nonlinear parabolic small-angle model of Kirby & Dalrymple (1983) are also presented for comparison. The small-angle model gives better results than the wide-angle does for this particular case. This may be explained that in the small-angle model the wave number, k_n, is determined locally while in the wide-angle model the wave number, K, is calculated by averaging k_c along the y-direction. Therefore, the wide-angle model is more sensitive to the imposed periodicity condition. Comparing our models against Dalrymple

et al.'s (1989) model and nonlinear parabolic model (Kirby & Dalrymple, 1983) the indices of agreement do not show large differences among them indicating that all the models work quite well for this particular case.

Section No.	M	Wide-Angle	Small-Angle	M	Dalrymple et al.	Parabolic
1	26	0.864	0.953	28	0.923	0.928
2	26	0.962	0.978	28	0.945	0.973
3	26	0.981	0.985	28	0.986	0.983
4	26	0.984	0.995	27	0.991	0.993
5	26	0.970	0.988	28	0.980	0.990
6	20	0.926	0.987	20	0.981	0.988
7	20	0.967	0.989	20	0.962	0.985
8	20	0.880	0.955	20	0.799	0.951
Total	190	0.977	0.991	199	0.983	0.990

Table 1: Indices of agreement for comparing the numerical model results against the measurements for the experiment of Berkhoff et al. (1982). "Parabolic" in last column refers to the nonlinear parabolic model of Kirby & Dalrymple (1983).

7.3   Wave focusing behind a circular shoal resting on a flat bottom

For the purpose of demonstrating the importance of the backward scattering field for large angles of incidence and the applicability of the wide-angle parabolic model for the case of a large angle of incidence over an uneven topography, we investigate the focusing of a monochromatic wave train behind a circular shoal resting on a flat bottom. Owing to the axisymmetry of the circular shoal, the wave focusing pattern behind the shoal should be independent of the angle of incidence.

The water depth for the first series of tests is given by

$$h = \begin{cases} h_0, & r > R \\ h_0 + \alpha - \beta\sqrt{1 - (x'/5)^2 - (y'/5)^2}, & r \leq R \end{cases} \qquad (7.18)$$

where $h_0 = 0.336m$ and $R = 4m$ is the radius of the shoal. The coordinates (x', y') with the origin at the crest of the shoal and x'-axis aligning with the incident wave direction are used and $r = \sqrt{x'^2 + y'^2}$. We denote the shoal with $\alpha = 0.12, \beta = 0.2$ in (7.18) as Case A and $\alpha = 0.18, \beta = 0.3$ as Case B. The corresponding shoal height at the crest for Case A is $0.08m$ and for Case B is $0.12m$. The same wave period and amplitude as those of Berkhoff et al. (1982) are used in the following numerical studies.

7.3.1 The Bremmer series solution for linear wave propagation

To obtain both forward and backward wave propagation fields, we shall solve equations (4.18) to (4.20) and generate the Bremmer series solution. In the following numerical computations, Neumann series (4.21) and (4.22) are truncated at $m = M$ according to the following condition:

$$|\eta^{\pm}_{n,M}(x)| \leq a_{max} \times 10^{-3} \qquad (n = 0, 1, \ldots, 2N - 1) \qquad (7.19)$$

where $a_{max} = \max\{a_0, \ldots, a_{2N-1}\}$.

The computational domain in the x-direction is $25m$ and in the y-direction is L, which has to satisfy the periodicity requirement (7.4). The marching step length is $\Delta x = 0.1m$ for all following numerical tests. For normal incidence, the computational domain (both Case A and B) is $L = 30m$, $N = 30$ (i.e. $\Delta y = 0.5m$) and the center of the shoal is located at $(x, y) = (15m, 7.5m)$; for incident wave with angle of incidence $\theta_0 = 60°$, $L = 89.60m$, $N = 90$ (i.e. $\Delta y = 0.498m$) for Case A and $L = 131.95m$, $N = 128$ (i.e. $\Delta y = 0.515m$) for Case B and the center of the shoal is located at $(x, y) = (7.5m, 7.5m)$. Figure 8(a,b) show the contour lines of wave amplitude normalized with respect to the incident amplitude for normal incidence. Solid lines indicate the results by the Bremmer series solution ($M = 2$ in (7.19) for Case A and $M = 3$ in (7.19) for Case B), while dotted lines indicate the results given by the linear wide-angle parabolic model. The comparison shows that for normal incidence, the backward scattering field indeed can be ignored and the linear wide-angle parabolic approximation can give very accurate results.
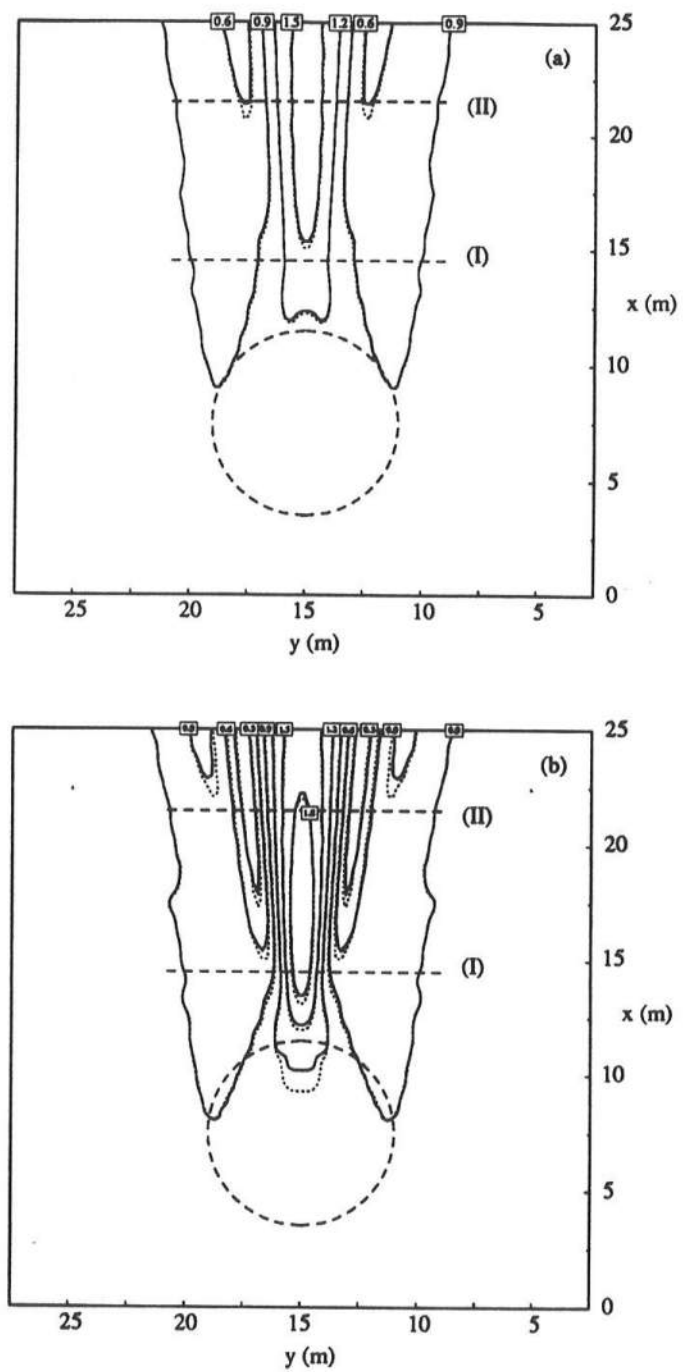
28

Figure 8: Contour lines of normalized amplitude for normal incidence: ——— Bremmer series solution; ···· linear wide-angle model. (a) Case A; (b) Case B.
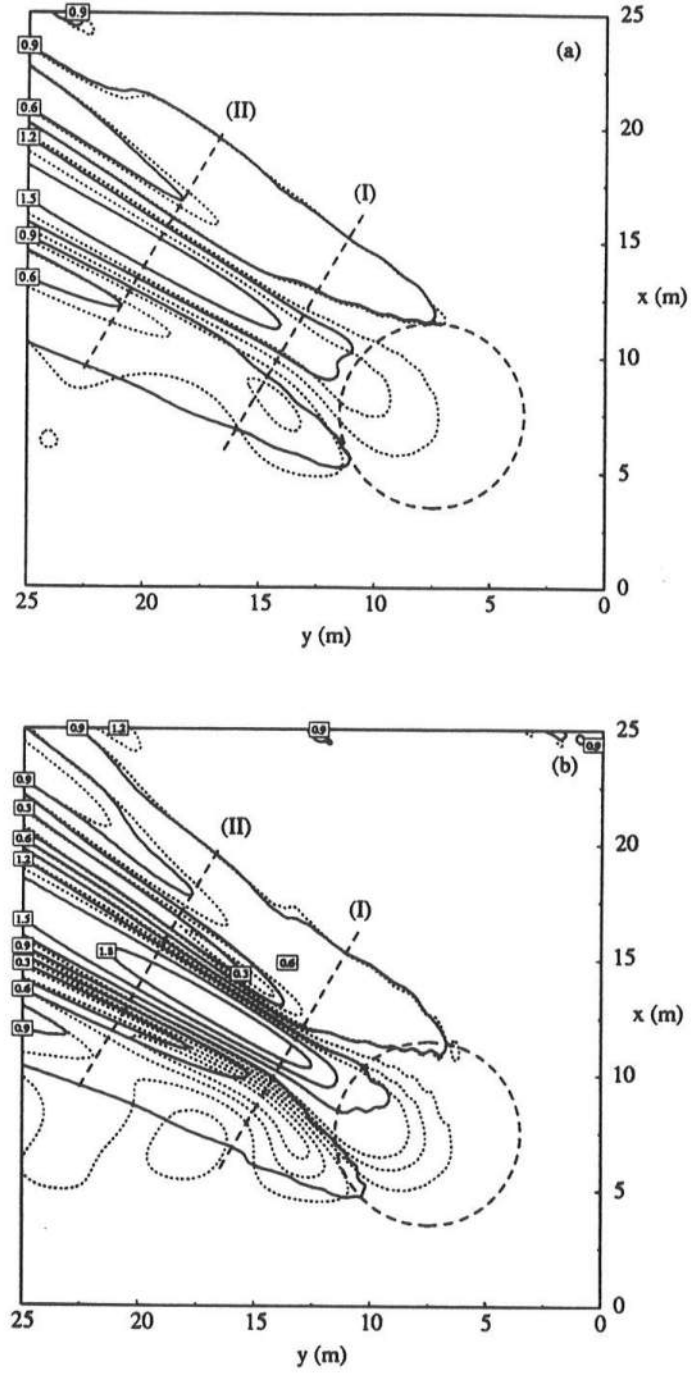
Figure 9: Contour lines of normalized amplitude for $\theta_0 = 60^o$: ——— Bremmer series solution; ···· linear wide-angle model. (a) Case A; (b) Case B.
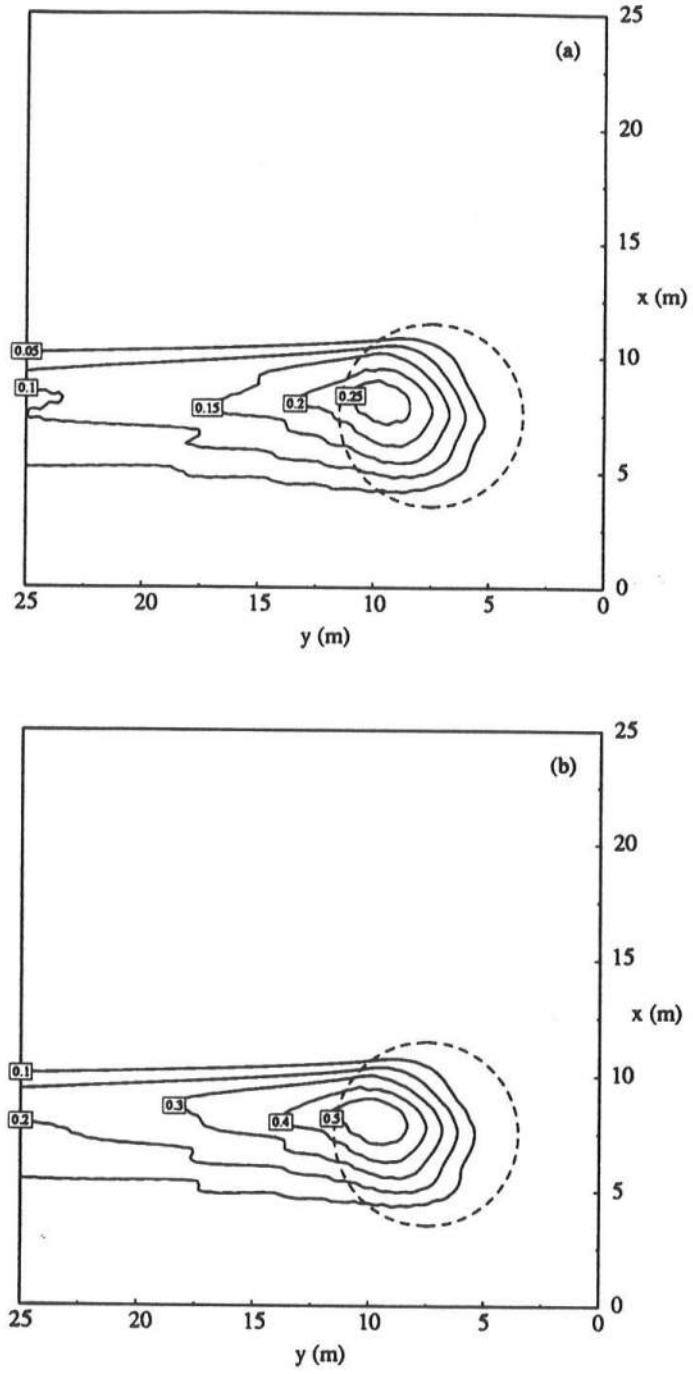
Figure 10: Contour lines of backward scattering wave amplitude normalized with respect to the incident amplitude for $\theta_0 = 60°$. (a) Case A; (b) Case B.

However, if the angle of incidence is large, the backward scattering is no longer small and should be taken into consideration. Figure 9(a,b) compare the contour pattern of
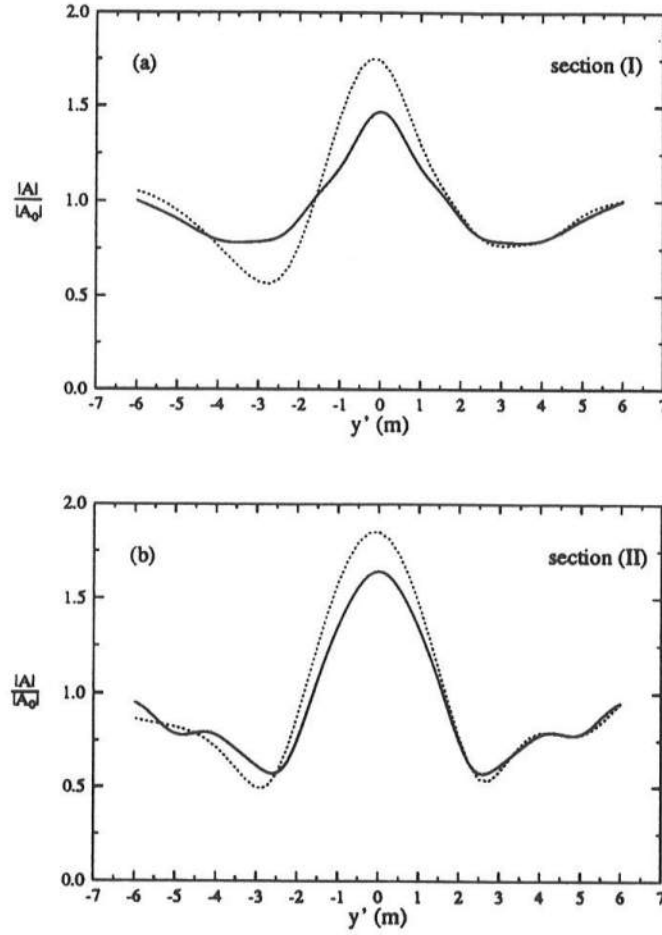
Figure 11: Comparison between normalized amplitude given by the linear wide-angle model along sections (I) and (II) for difference angles of incidence for Case A: —— $\theta_0 = 0°$; $\cdots\cdots$ $\theta_0 = 60°$.

the Bremmer series solution results for $\theta_0 = 60°$ (solid lines; $M = 3$ for Case A and $M = 4$ for Case B) against the pattern of wide-angle parabolic approximation (dotted lines). The difference is quite obvious. Comparing figures 8 and 9, we observe that the Bremmer series solutions, which include the backward scattering field, give almost the same focusing patterns behind the shoal for $\theta_0 = 60°$ as those for $\theta_0 = 0°$. To show the region in which the backward scattering field is important, we plotted the contours for the

backward scattering amplitude ($\phi_n^-(x) = \sum_{j=0}^{2N-1} Q_{n,j}\eta_j^-(x)$) normalized with respect to
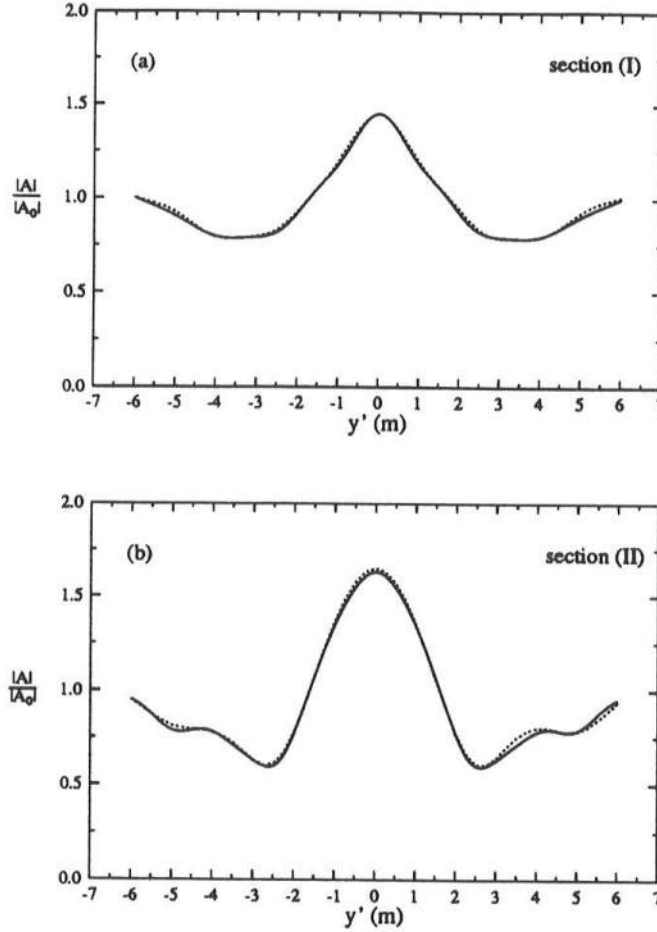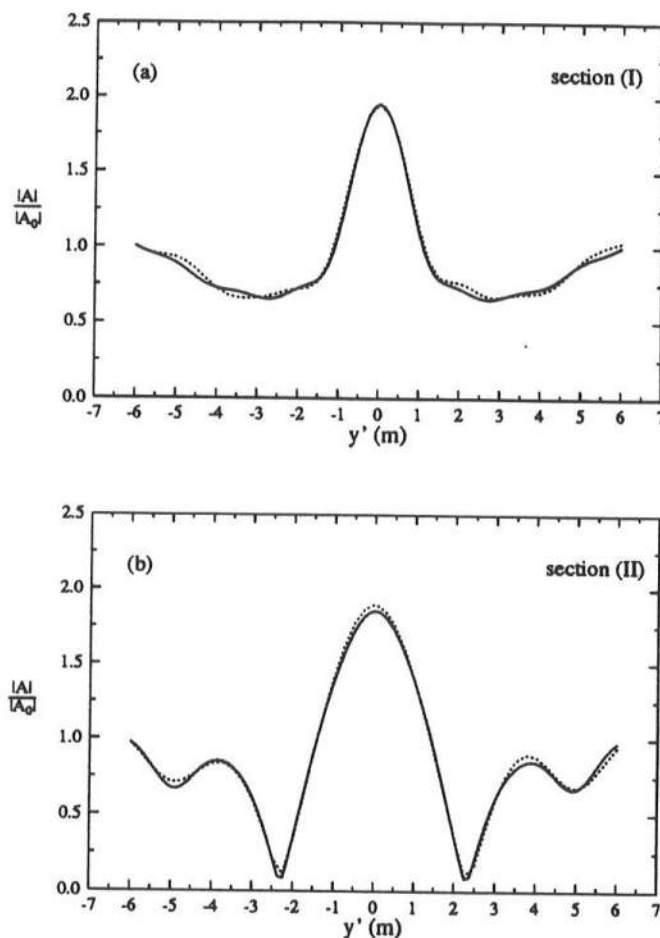

Figure 12: Comparison between normalized amplitude given by the Bremmer series solution along sections (I) and (II) for different angles of incidence for Case A: —— $\theta_0 = 0°$; $\cdots\cdots$ $\theta_0 = 60°$.

the incident amplitude in figure 10(a,b). These figures show that the backward scattering is important only inside the narrow strip region as shown in the figures, with maximum value about 0.28 for Case A and 0.59 for Case B located on the left-hand side near the center of the shoal. Outside this region the backward scattering can be ignored. For more quantitative comparison, we compare the wave amplitude along sections (I) and (II) which are $7m$ and $14m$ away from the shoal crest. Figure 11(a,b) show the results given by wide-angle model for Case A with $\theta_0 = 0°$ and $60°$. Solid lines indicate the results for normal

incidence and dotted lines indicate the results for $\theta_0 = 60°$. Except on the right-hand side, the difference is large. Figure 12(a,b) and 13(a,b) show the Bremmer series results

Figure 13: Comparison between normalized amplitude given by the Bremmer series solution along sections (I) and (II) for different angles of incidence for Case B: —— $\theta_0 = 0°$; ···· $\theta_0 = 60°$.

for $\theta_0 = 0°$ and $\theta_0 = 60°$ for Case A and B along sections (I) and (II). Again, solid lines indicate the results for $\theta_0 = 0°$ and the dotted lines represent the results for $\theta_0 = 60°$; the agreement between two different angles of incidence is excellent for both cases. Therefore, the Bremmer series solution which we constructed can be used to simulate the linear wave propagation accurately for large angles of incidence, and the rate of convergence rate is very fast for all examples given here ($M \leq 4$).

7.3.2 Test of nonlinear wide-angle parabolic model for large angles of incidence

Three different angles of incidence are used to test the nonlinear wide-angle parabolic model: $\theta_0 = 0°, \theta_0 = 45°$ and $\theta_0 = 60°$. The computational domain in the x-direction is still $25m$ and in the y-direction is L, which has to satisfy the periodicity requirement (7.4). The marching step length is $\Delta x = 0.1m$ for all following numerical tests. For the normal incident wave, $L = 25m$, $N = 25$ (i.e. $\Delta y = 0.5m$); the center of the shoal is located at $(x, y) = (12.5m, 7.5m)$. For the incident wave with $\theta_0 = 45°$, $L = 63.84m$, $N = 64$ (i.e. $\Delta y = 0.499m$); the center of the shoal is at $(7.5m, 7.5m)$. For the incident wave with $\theta_0 = 60°$, $L = 94.48m$, $N = 96$ (i.e. $\Delta y = 0.492m$); the center of the shoal is also located at $(x, y) = (7.5m, 7.5m)$. For Case A, the contours of the normalized amplitude with respect to the incident wave amplitude are shown in figure 14(a,b,c) for each angle of incidence. The overall wave focusing pattern behind the shoal for $\theta_0 = 45°$ is very similar to that for $\theta_0 = 0°$, while the wave pattern for $\theta_0 = 60°$ has some distortions on the left side of the centerline. For more quantitative comparison, the variations of the normalized amplitude along sections (I) and (II) are plotted in figure 15(a,b). Solid lines indicate the results for $\theta_0 = 0°$ while circles and triangles indicate the results for $\theta_0 = 45°$ and $\theta_0 = 60°$ respectively. Along section (I), which is just behind the shoal, the agreement among the results of three different angles of incidence is very good; along section (II), the results for $\theta_0 = 45°$ still agree very well with those for $\theta_0 = 0°$, but on the left-hand side of the centerline, the results for $\theta_0 = 60°$ do not agree very well with those for $\theta_0 = 0°$.

The height of the shoal crest in Case A is about 1/4 of the water depth on flat bottom. In order to examine the effect of the magnitude of the bottom variation, we have tested the model for a higher shoal—Case B which is about 1/3 of the water depth on the flat bottom. The same computational parameters are used as the previous tests. Figure 16(a,b,c) show the amplitude variations for $\theta_0 = 0°$, $\theta_0 = 45°$ and $\theta_0 = 60°$ respectively. The wave pattern for $\theta_0 = 45°$ still looks very similar to that for $\theta_0 = 0°$. But distortion of the focusing pattern for the 60° incidence becomes severe, and the wave amplitude near the centerline

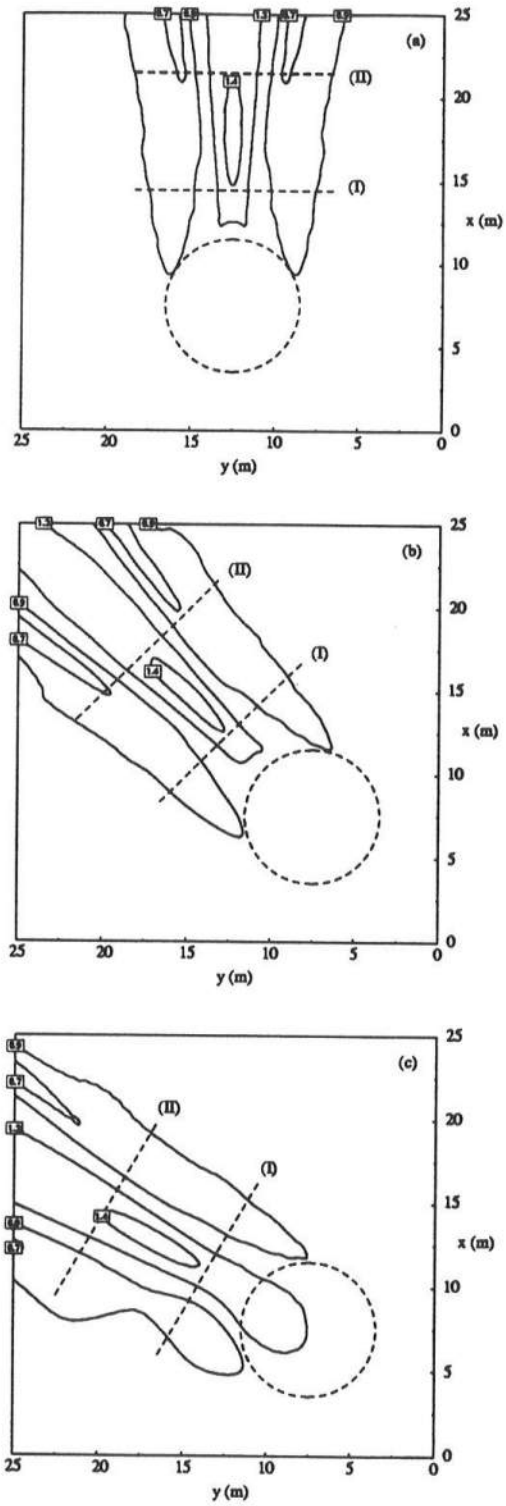Figure 14: Wave focusing pattern predicted by the nonlinear wide-angle model for Case A: (a) $\theta_0 = 0^o$; (b) $\theta_0 = 45^o$; (c) $\theta_0 = 60^o$.
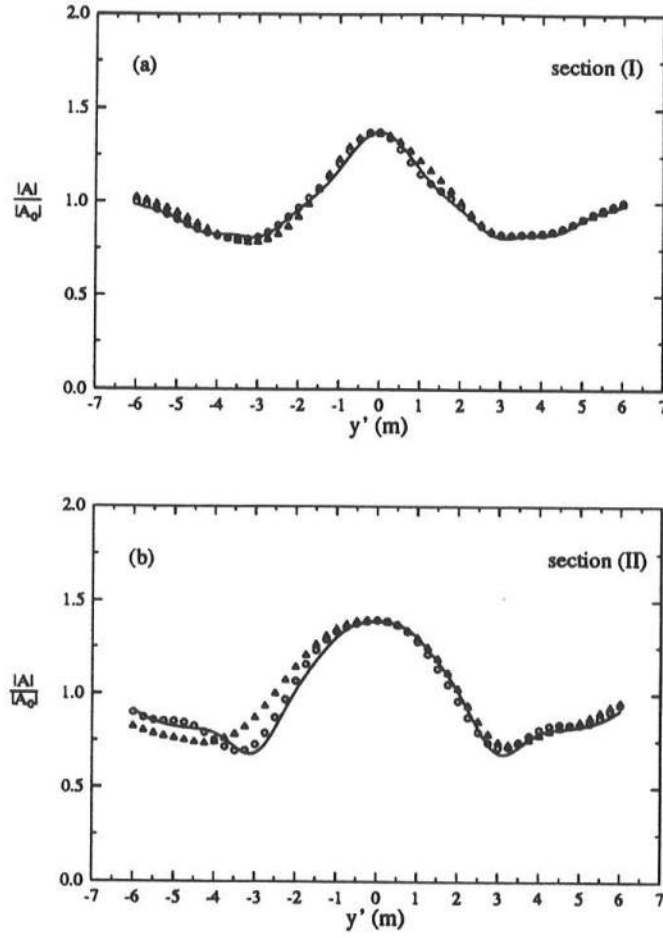
of focusing tends to be over predicted.

Figure 15: Quantitative comparison among the results of normalized amplitude given by the nonlinear wide-angle model along section (I) and (II) for different angles of incidence : —— $\theta_0 = 0°$; ∘ ∘ ∘ $\theta_0 = 45°$; △△△ $\theta_0 = 60°$.

The above numerical tests show that for a large angle of incidence ($> 45°$), to obtain accurate results, the backward scattering field can not be ignored. Intuitively, the wave field in the constant depth region before the shoal should be affected by the presence of the shoal if a large angle of incidence is modelled. The higher the shoal is, the greater this effect is. But this is not detected by the wide-angle model since it does not include backward scattering wave. Comparing figure 14 and its counterpart figure 16, we found that the greater the bottom variation in the y-direction, the bigger the error of the nonlinear wide-
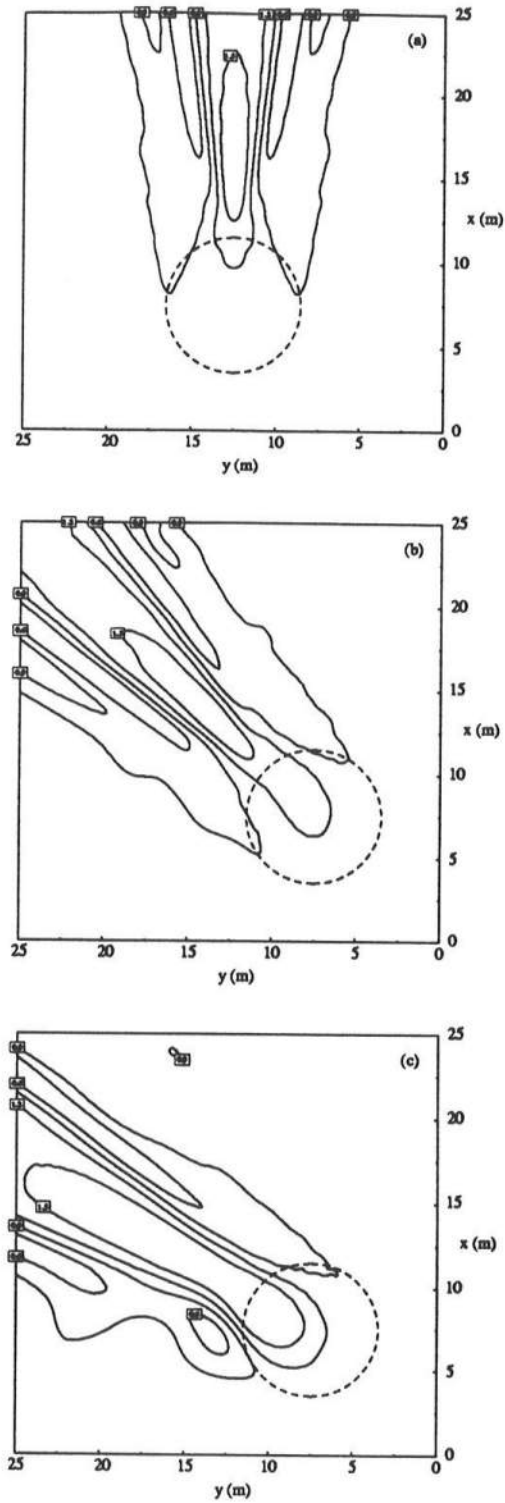
Figure 16: Wave focusing pattern predicted by the nonlinear wide-angle model for Case B: (a) $\theta_0 = 0°$; (b) $\theta_0 = 45°$; (c) $\theta_0 = 60°$.

angle parabolic model for the same angle of incidence. Comparing the results from linear and nonlinear parabolic wide-angle model (see figure 9a and 14c), we found that since the nonlinearity increases the diffraction effect, for a large angle of incidence the contribution from the backward modes for nonlinear waves is not as great as that for linear waves.

8   Concluding Remarks

Using the pseudospectral Fourier approach, Bremmer series solution which includes both the forward and backward scattering fields is obtained for linear waves and "wide-angle" and "small-angle" parabolic wave propagation models are developed. The effects of non-linearities due to finite wave amplitudes, bottom friction and wave breaking are included directly in the models. The success for deriving the Bremmer series solution and wide-angle parabolic model hinges on the fact that the coupling matrix D_2:

$$[D_2]_{n,j} = \frac{d^2 g_j(y_n)}{dy^2}$$

is a real symmetric matrix when the wave field can be assumed to be periodic in alongshore direction. This guarantees the existence of a global transformation matrix Q used to decompose the wave field into a series of propagation modes which consist of a complete discrete angular spectrum. If other kinds of interpolation functions are used to relax the limitation of periodic lateral boundary condition, such as Chebyshev polynomials, this property may not be preserved. Then only the small-angle model can be derived.

For linear waves, all the backward propagation modes are included in the Bremmer series solution. Through a numerical example it is shown that the backward propagation modes could become significant when the angle of incidence is large. This is true even if the reflection is negligible. In the Bremmer series solution because the entire discrete angular spectrum is included in both forward and backward wave fields, the converged numerical solution satisfies the original linear mild-slope equation. Therefore, not only the refraction and diffraction, but also the reflection are included in the solution.

39

For nonlinear waves, only the forward propagation modes are included. This is because all the nonlinear effects considered in the nonlinear mild-slope equation are derived, either analytical or empirically, from the assumption that waves are forward propagating. A rigorous derivation of a nonlinear mild-slope equation is needed. Questions concerning the splitting of nonlinear effects, such as breaking, bottom friction and finite amplitude, between forward and backward propagation modes are interesting topics for future research.

Acknowledgement

Appendix

Considering the multiplicity of the eigenvalues of D_2 and noting that $\lambda_n^2 = n^2$, the directions of forward propagation modes can be explicitly given as (from (4.16))

$$\theta_n = \tan^{-1}\left[\frac{\left(\frac{2\pi}{L}\right)n}{\sqrt{K^2 - \left(\frac{2\pi}{L}\right)^2 n^2}}\right] \qquad (-N+1 \leq n \leq N) \qquad \text{(A.1)}$$

If the angle of incidence coincides with one of θ_n in (A.1), say θ_M $(-N+1 \leq M \leq N)$

$$\theta_M = \tan^{-1}\left[\frac{\left(\frac{2\pi}{L}\right)M}{\sqrt{K_0^2 - \left(\frac{2\pi}{L}\right)^2 M^2}}\right] \qquad \text{(A.2)}$$

40

where $K_0 = K(0)$, then the incident wave can be expressed as

$$\xi(0, y) = \xi_0 \exp\{iK_0 y \sin \theta_M\} \tag{A.3}$$

with ξ_0 being a constant.

The initial values for $\psi_j(x)$ $(j = 0, 1, \ldots, 2N - 1)$ are given by (3.7)

$$\psi_j(0) = \xi_0 \exp\{iK_0 \sin \theta_M \frac{L}{2\pi} \bar{y}_j\} = \xi_0 \exp\{i\frac{2\pi}{L} M \frac{L}{2\pi} \bar{y}_j\}$$
$$= \xi_0 [\cos(M\bar{y}_j) + i \sin(M\bar{y}_j)] \tag{A.4}$$

From (7.3) the initial values for $\eta_m(0)$ become

$$\eta_m(0) = \sum_{j=0}^{2N-1} Q_{j,m} \psi_j(0) \qquad (m = 0, 1, \ldots, 2N - 1) \tag{A.5}$$

Because the column vectors of Q in (4.6) are mutually orthogonal, the summation in (A.5) can be expressed explicitly as the follows:

$$\eta_m(0) = \begin{cases} \sqrt{2N}\, \xi_0, & m = 0 \\ 0, & \text{otherwise} \end{cases} \quad ; \qquad \text{if} \quad M = 0;$$

$$\eta_m(0) = \begin{cases} \sqrt{2N}\, \xi_0, & m = 2N - 1 \\ 0, & \text{otherwise} \end{cases} \quad ; \qquad \text{if} \quad M = N; \tag{A.6}$$

$$\eta_m(0) = \begin{cases} \sqrt{N}\, \xi_0, & m = 2|M| - 1 \\ \text{sgn}(M)i\sqrt{N}\, \xi_0, & m = 2|M| \\ 0, & \text{otherwise} \end{cases} \quad ; \quad \text{if} \quad 1 \leq |M| \leq N - 1.$$

The linear version of (4.14) has an analytical solution if h is a function of x only, i.e.

$$\eta_m(x) = \eta_m(0) \left[\frac{K_0^2 - (\frac{2\pi}{L})^2 \lambda_m^2}{K^2 - (\frac{2\pi}{L})^2 \lambda_m^2}\right]^{1/4} \exp\left\{i \int_0^x \sqrt{K^2 - \left(\frac{2\pi}{L}\right)^2 \lambda_m^2}\, dx\right\} \tag{A.7}$$

41

Thus

$$\psi_n(x) = \sum_{m=0}^{2N-1} Q_{n,m} \eta_m(x)$$

$$= Q_{n,0}\eta_0 + \sum_{m=1}^{N-1} [Q_{n,2m-1}\eta_{2m-1} + Q_{n,2m}\eta_{2m}] + Q_{n,2N-1}\eta_{2N-1} \qquad (A.8)$$

Substituting (A.6) and (A.7) into (A.8), we have

$$\psi_n(x) = \xi_0 \left[\frac{K_0^2 - (\frac{2\pi}{L})^2 M^2}{K^2 - (\frac{2\pi}{L})^2 M^2} \right]^{1/4} \exp \left\{ i \int_0^x \sqrt{K^2 - \left(\frac{2\pi}{L}\right)^2 M^2} \, dx + iM\bar{y}_n \right\} \qquad (A.9)$$

Therefore

$$\xi(x,y) = \xi_0 \left[\frac{K_0^2 - (\frac{2\pi}{L})^2 M^2}{K^2 - (\frac{2\pi}{L})^2 M^2} \right]^{1/4} \exp \left\{ i \int_0^x \sqrt{K^2 - \left(\frac{2\pi}{L}\right)^2 M^2} \, dx + i\frac{2\pi}{L}My \right\} \qquad (A.10)$$

and

$$\frac{|\zeta|}{|\zeta_0|} = \frac{|\phi|}{|\phi_0|} = \left| \frac{\xi/\sqrt{CC_g}}{\xi_0/\sqrt{C_0 C_{g0}}} \right| = \left\{ \frac{[K_0^2 - (\frac{2\pi}{L})^2 M^2] C_0^2 C_{g0}^2}{[K^2 - (\frac{2\pi}{L})^2 M^2] C^2 C_g^2} \right\}^{1/4}$$

$$= \left[\frac{\cos\theta_M K_0 C_0 C_{g0}}{\sqrt{1 - (\frac{2\pi}{L})^2 \frac{M^2}{K^2}} K C C_g} \right]^{1/2} \qquad (A.11)$$

Since $k_y = 2\pi M/L$ remains constant, we have

$$\sqrt{1 - \left(\frac{2\pi}{L}\right)^2 \frac{M^2}{K^2}} = \cos\theta \qquad (A.12)$$

Substituting (A.12) into (A.11) and neglecting the difference between $K = k_c$ and k (see(2.8)), we have

$$\frac{|\zeta|}{|\zeta_0|} = \left[\frac{\cos\theta_M C_{g0}}{\cos\theta C_g} \right]^{1/2} \qquad (A.13)$$

which is the well-known refraction formula and can also be derived from the ray theory.

42

References

[1] Atkinson, F.V. 1960 Wave propagation and the Bremmer series. Journal of Mathematical Analysis and Applications, 1, pp. 255-276.

[2] Berkhoff, J.C.W. 1972 Computation of combined refraction-diffraction. Proc. 13th Conf. Coastal Eng. ASCE 1: pp471-490.

[3] Berkhoff, J.C.W. 1976 Mathematical models for simple harmonic linear water waves, wave diffraction and refraction. Delft Hydraulics Laboratory, Publication No. 163.

[4] Berkhoff, J.C.W., Booij, N. & Radder, A.C. 1982 Verification of numerical wave propagation models for simple harmonic linear waves. Coastal Engrg., 6, pp. 255-279.

[5] Booij, N. Gravity waves on water with non-uniform depth and current. Thesis presented to the Technical University of Delft, The Netherlands in 1981, in partial fulfillment of the requirements for the degree of Doctor of Philosophy.

[6] Dalrymple, R.A. , Kirby, J.T. & Hwang, P.A. 1984 Wave diffraction due to area of energy dissipation. J. Waterway, Port, Coastal and Ocean Engrg., 110(1), pp. 67-79.

[7] Dalrymple, R.A. & Kirby, J.T. 1988 Models for very wide-angle water waves and wave diffraction. J. Fluid Mech., 192, pp. 33-50.

[8] Dalrymple, R.A., Suh, K.D., Kirby, J.T. & Chae, J.W. 1989. Models for very wide-angle water waves and wave diffraction. Part 2. Irregular bathymetry. J. Fluid Mech., 201, pp. 299-322.

[9] Dally, W.R., Dean, G.D., & Dalrymple, R.A. 1985 Wave height variation across beaches of arbitrary profile. J. Geophys. Res., Vol. 90, No. C6, pp. 11917-11927.

[10] Dean, R.G. 1977 Equilibrium beach profiles: U.S. Atlantic and Gulf Coasts. Ocean Engineering Report No. 12, Univ. of Delaware, Newark, Delaware.

[11] Dingemans, M.W. 1983 Verification of numerical wave propagation models with field measurements: CREDIZ verification. Report W488 part 1, Delft Hydraulics Laboratory.

[12] Dingemans, M.W. 1985 Surface wave propagation over an uneven bottom: Evolution of two-dimensional horizontal models. Report W301, part 5, Delft Hydraulics Laboratory.

[13] Dodd, N. 1991 Reflective properties of parabolic approximations in shallow water wave propagation. SIAM J. Appl. Math., Vol. 51, No. 3, pp. 635-657.

[14] Gottlieb, D., Hussaini, M.Y. & Orszag, S.A. 1984 Introduction: Theory and applications of spectral methods. In Spectral Methods for Partial Differential Equations (ed. by Voigt, R.G., Gottlieb, D. & Hussaini, M.Y.), SIAM, Philadelphia, pp. 1-54.

[15] Kirby, J.T. & Dalrymple, R.A. 1983 A parabolic equation for the combined refraction-diffraction of Stokes waves by mildly varying topography. J. Fluid Mech., 136, pp. 453-466.

[16] Kirby, J.T. & Dalrymple, R.A. 1986 Modeling Waves in surf zones and around islands. J. Waterways, Port, Coastal and Ocean Engineering, 112(1), pp. 78-93.

[17] Liu, P. L.-F. & Tsay, T.K. 1983 On weak reflection of water waves. J. Fluid Mech., 131, pp. 59-71.

[18] Liu, P. L.-F. & Tsay, T.K. 1984 Refraction-diffraction model for weakly nonlinear water waves. J. Fluid Mech., 141, pp. 265-274.

[19] Liu, P. L.-F. & Tsay, T.K. 1985 Numerical prediction of wave transformation. J. Waterways, Port, Coastal and Ocean Engrg., 111(5), pp. 843-855.

[20] Liu, P. L.-F. 1986 Viscous effects on the evolution of Stokes waves. J. Waterway, Port, Coastal and Ocean Engrg., 112(1), pp. 55-63.

[21] Liu, P. L.-F. 1990 Wave transformation. In the SEA: Ocean engineering science, John Wiley & Sons, Vol. 9, pp. 27-63.

[22] McMaken, H. 1986 On the convergence of the Bremmer series for the Helmholtz equation in 2-D. Wave Motion, 8, pp. 277-283.

[23] Panchang, V.G. & Kopriva, D.A. 1989 Solution of two-dimensional water-wave propagation problems by Chebyshev collocation. Math. Comput. Modeling, 12(6), pp. 625-640.

[24] Radder, A.C. 1979 On the parabolic equation method for water-wave propagation. J. Fluid Mech., 95, pp. 159-176.

[25] Smith, R. & Sprinks, T. 1975 Scattering of surface waves by a conical island. J. Fluid Mech., 72, pp. 373-384.

[26] Suh, K.D., Dalrymple, R. A. & Kirby, J.T. 1990 An angular spectrum model for propagation of Stokes waves. J. Fluid Mech., 221, pp. 205-232.

[27] Willmott, C.J. 1981 On the validation of models. Phys. Geog. 2, pp. 184-194.

[28] Yue, D.K.P. & Mei, C.C. 1980 Forward diffraction of Stokes waves by a thin wedge. J. Fluid Mech., 99, pp. 33-55.